

THESIS

IPE: EVALUATION OF ORTHOTROPIC ELASTIC PROPERTIES AND ITS APPLICATION
IN ROADSIDE BARRIERS

Submitted by

Robert Lankford

Department of Civil and Environmental Engineering

In partial fulfillment of the requirements

For the Degree of Master of Science

Colorado State University

Fort Collins, Colorado

Summer 2016

Master's Committee:

Advisor: Paul Heyliger

Rebecca Atadero
Scott Glick

Copyright by Robert Lankford 2016

All Rights Reserved

ABSTRACT

IPE: EVALUATION OF ORTHOTROPIC ELASTIC PROPERTIES AND ITS APPLICATION IN ROADSIDE BARRIERS

Roadside barriers are the primary structural safety device on surface roads. They can be made from any material as long as they can absorb the energy involved in an impact scenario. One material that has that potential is Ipe. Ipe is a hardwood material that has relatively high strength compared to common structural woods. Despite its high strength, the 9 independent material properties for Ipe has not studied in the literature. In this paper, those material properties are determined with various tests. With the material properties, dynamic finite element analyses were done with seven different roadside barrier configurations and were then compared to the performance of the commonly used steel W-beam barrier. Ipe showed great potential with certain configurations, but with a much higher cost. Realistic implementation of Ipe in roadside barriers would be more beneficial for roads with lower speed limits, thus lowering that cost.

TABLE OF CONTENTS

ABSTRACT.....	ii
LIST OF TABLES.....	v
LIST OF FIGURES.....	vi
Chapter 1 – Introduction.....	1
1.1 Background.....	1
1.2 Aims and Objectives.....	3
Chapter 2 - Literature Review.....	4
2.1 Introduction.....	4
2.2 Ipe and CFRP Engineering Properties.....	4
2.2.1 Wood Mechanics.....	4
2.2.2 Ipe.....	9
2.2.3 Fiber Reinforced Polymers.....	11
2.3 Roadside Barriers.....	14
2.3.1 Introduction.....	14
2.3.2 Testing and Criteria.....	14
2.3.3 Rail Section Developments.....	19
2.4 Modeling of Rails and Barriers.....	22
2.4.2 Experiments and Models.....	24
Chapter 3 - Methodologies and Results.....	29
3.1 Introduction.....	29

3.2 Material Testing	29
3.2.1 Samples	29
3.2.2 Static three-point bending	30
3.2.3 Static three-point bending with CFRP	33
3.2.4 Compression Tests	35
3.2.5 Impact Resonance Testing	40
3.2.6 Resonant Ultrasound Spectroscopy	41
3.2.5 Validation.....	43
3.3 Modelling of Prototype Barriers	45
3.3.1 Geometry and Meshing.....	46
3.3.2 Analysis Set-up	51
3.3.3 Constraints, Loading, and Boundary Conditions	52
3.3.4 Railing Configurations.....	53
3.3.5 Model Results and Discussion	56
Chapter 4 – Conclusion.....	69
References	73
Appendix A – Additional Figures.....	79

LIST OF TABLES

Table 1: Ipe Properties (FPL 2010)	9
Table 2: Three-Point Bending Results for Ipe Specimens	32
Table 3: Dry Fiber and Epoxy Material Properties.....	33
Table 4: FRP Composite Laminate Properties.....	34
Table 5: Three-Point Bending for Ipe with CFRP Specimens.....	35
Table 6: Mean dimensions of test specimens	36
Table 7: Material Property Results from Compression Tests.....	39
Table 8: Material Property Results Comparison to Common NA Woods (FPL 2010).....	40
Table 9: Dimensions of Impact Resonance Specimens	41
Table 10: Initial Validation Modelling Results, with Varying Moduli Inputs	45
Table 11: Validation Modelling Results, with Adjusted Local Material Axes.....	45
Table 12: Impact Scenarios.....	52
Table 13: Model Rail Configurations	55
Table 14: Maximum Displacement Results	61
Table 15: Maximum Stress Results	62
Table 16: Comparison of Ipe-A and Ipe-A-CFRP	66

LIST OF FIGURES

Figure 1 – (Source: Wood Handbook).....	5
Figure 2: Wood Preparation Setup (Source: Fyfe)	13
Figure 3 – Wood Preparation Close-up (Source: Fyfe)	13
Figure 4: Flexible Barrier System: Three-Strand Cable (Source: blog.udot.utah.gov)	17
Figure 5: Semi-Rigid Barrier System: Strong Post W-Beam (Source: safety.fhwa.dot.gov).....	17
Figure 6: Rigid Barrier System: Concrete (Source: safety.fhwa.dot.gov).....	18
Figure 7: Cross-Section of “CGR10” Composite Configuration (Source: Bank 2001)	20
Figure 8: Wood/FRP Composite Cross-Section Developed by Davids et al. (Davids 2006).....	22
Figure 9: FEA Model of “G4-1S” W-beam guardrail with LS-DYNA (Whitworth 2004).....	26
Figure 10: Portable Water-Filled Road Safety Barrier Schematic (Thiyahuddin 2014)	27
Figure 11: Post-Processing Analysis via Abaqus (Shen 2008).....	28
Figure 12: Instron UTM with Loading Mechanism and Ipe Specimen	30
Figure 13: Load vs Displacement at Midspan	31
Figure 14: Ipe 3-pt Bending Specimens. (1 on top, 3 on bottom)	32
Figure 15: Compression Test Sample Orientations – 1	36
Figure 16: Compression Test Sample Orientations – 2	36
Figure 17: Longitudinal Stress vs Strain.....	37
Figure 18: Radial Stress vs. Strain.....	38
Figure 19: Tangential Stress vs. Strain	38
Figure 20: RUS Analysis between 130 Hz and 170 Hz.....	42

Figure 21: RUS Analysis between 200 Hz and 240 Hz.....	42
Figure 22: RUS Analysis of Beech Sample as published by Longo et al. (2012)	43
Figure 23: Coarse Mesh of Beam Validation Model	44
Figure 24: Fine Mesh of Beam Validation Model	44
Figure 25: Cross-section of Steel W-beam	47
Figure 26: CFRP Strip (90mm) Geometry.....	48
Figure 27: Post and Offset Block Geometry.....	48
Figure 28: Soil Geometry.....	49
Figure 29: Vehicle Geometry.....	50
Figure 30: Top-down (Plan) View of Overall Model with Steel W-Beam Railing.....	51
Figure 31: General View of Overall Model with Steel W-Beam Railing.....	51
Figure 32: Steel W-Beam – Displacement versus Time.....	57
Figure 33: Ipe-A – Displacement versus Time	57
Figure 34: Ipe-A-CFRP – Displacement Versus Time	58
Figure 35: Ipe-D – Displacement Versus Time	58
Figure 36: Ipe-E – Displacement Versus Time.....	59
Figure 53: Performance Comparison – 1,500 kg @ 100km/hr.....	63
Figure 54: Performance Comparison – 895 kg @ 100km/hr.....	63
Figure 55: Performance Comparison – 895 kg @ 70km/hr.....	64
Figure 56: Performance Comparison – 895 kg @ 50km/hr.....	64
Figure 37: Impact Simulation – Steel W-beam – 1500kg vehicle @ 100km/hr.....	80
Figure 38: Impact Simulation – Steel W-beam – 895kg vehicle @ 100km/hr.....	80

Figure 39: Impact Simulation – Steel W-beam – 895kg vehicle @ 70km/hr.....	81
Figure 40 Impact Simulation – Steel W-beam – 895kg vehicle @ 50km/hr.....	81
Figure 41: Impact Simulation – IpeA – 1500kg vehicle @ 100km/hr.....	82
Figure 42: Impact Simulation – IpeA – 895kg vehicle @ 100km/hr.....	82
Figure 43: Impact Simulation – IpeA – 895kg vehicle @ 70km/hr.....	83
Figure 44: Impact Simulation – IpeA – 895kg vehicle @ 50km/hr.....	83
Figure 45: Impact Simulation – IpeD – 1500kg vehicle @ 100km/hr.....	84
Figure 46: Impact Simulation – IpeD – 895kg vehicle @ 100km/hr.....	84
Figure 47: Impact Simulation – IpeD – 895kg vehicle @ 70km/hr.....	85
Figure 48: Impact Simulation – IpeD – 895kg vehicle @ 50km/hr.....	85
Figure 49: Impact Simulation – IpeE – 1500kg vehicle @ 100km/hr.....	86
Figure 50: Impact Simulation – IpeE – 895kg vehicle @ 100km/hr.....	86
Figure 51: Impact Simulation – IpeE – 895kg vehicle @ 70km/hr.....	87
Figure 52: Impact Simulation – IpeE – 895kg vehicle @ 50km/hr.....	87

CHAPTER 1 – INTRODUCTION

1.1 BACKGROUND

Bridge and guard rails are types of roadside barriers that are commonplace alongside the vast network of interstates, highways, and roads with the primary purpose of roadside safety. These barriers may be constructed from a variety of materials, including steel, concrete, wood, cables, composites, and more. They also are constructed into different shapes and sizes. Numerous theoretical and empirical studies have been conducted over the past half century to determine roadside barrier performance with varying materials and configurations.

Roadside barriers, as listed by the American Association of State Highway and Transportation Officials (AASHTO), fall under three main categories: flexible, semi-rigid, and rigid systems. As their names suggest, the categories reflect the intended behavior of the barrier. Roadside barriers are also classified based on performance guidelines as outlined by the National Cooperative Highway Research Program (NCHRP) Report 350. In this report, there are 6 test levels which a barrier can be classified: TL-1 to TL-6. A TL-3 designation is the minimum required for highways and interstates, requiring proper redirection of a vehicle, lack of flying debris, and more while maintaining specific speeds for various vehicle types.

According to AASHTO, some of the commonly used roadside barriers are the strong-post W-beam, the three-strand cable, and concrete barriers. The strong-post W-beam is a semi-rigid system and is the most common roadside barrier. Advantages for the strong-post W-beam roadside barrier are its TL-3 designation and its capability to remain functional after minor

collisions (AASHTO 2002). Three-strand cable barriers are flexible systems and consists of, as the name implies, three cables tied to posts. The three-strand cable system also carries the TL-3 designation (AASHTO 2002). Concrete barriers are rigid systems with various shapes. Designations of TL-4 and TL-5 are typically assigned to concrete barriers (AASHTO 2002).

Any material can be utilized in a barrier as long as the overall structure satisfies the evaluation criteria listed by NCHRP. Even though there have been many studies in the field, there are many other materials that are yet to be studied in such an application. Ipe, a Brazilian hardwood, is one of these materials that could possess potential. The Ipe designation is used for the genus *Tabebuia* and is found in the majority of Latin America (Wood Handbook 2010). The wood is known for its high density, hardness, and strength in relation to other woods. The density is approximately 1,025 kg m⁻³ (64 lb ft⁻³) at 12% moisture content. Ipe is also highly resistant to decay and insects. Currently, Ipe is primarily used for heavy-duty applications such as flooring in trucks and boxcars. Other uses include deckings, railroad crossties, decorative veneers, etc. The combination of Ipe's sturdy properties, natural environmental resistance, and visual appeal, shows potential for its use in a roadside barrier.

Another material that has just recently been studied in roadside barrier applications are fiber-reinforced polymers (FRP). Typically, many railings consisting solely of wood would not have the strength required to satisfy NCHRP's criteria. To compensate, a steel plate could be installed on the back tensile face of the railing to provide the extra strength that is needed. Fiber-reinforced polymers have a strength to weight ratio that is significantly higher than that of steel. Thus, using FRP in the same manner as the steel plate shows potential. Davids et al. (2006)

studied one such application using glass FRP (GFRP) with commonly found woods in North America, such as the red maple. They concluded that their design “has a high probability of passing a TL-3 crash test and gaining acceptance for use in highway applications under the requirements of NCHRP Report 350” (Davids 2005).

1.2 AIMS AND OBJECTIVES

This research project aims to study the material properties of Ipe and determine potential applications in roadside barrier configurations. Fiber-reinforced polymers will also be implemented. Analysis will be compared with commonly used barriers, such as the semi-rigid W-beam steel barrier to determine their viability and potential in obtaining various NCHRP’s evaluation criteria.

This research has two main parts. Firstly, specimens of Ipe will be obtained from a local supplier and tests will be performed to determine various engineering properties. Secondly, rail models will be created to detail the material’s response in an impact based simulation using different configurations. Overall conclusions will be presented relative to the potential use of Ipe as a barrier material.

CHAPTER 2 - LITERATURE REVIEW

2.1 INTRODUCTION

A literature review was conducted to gather published data for Ipe and fiber-reinforced materials, general guidelines and design specifications for longitudinal rail systems, and published articles regarding rail system configurations.

2.2 IPE AND CFRP ENGINEERING PROPERTIES

2.2.1 Wood Mechanics

One can easily search for claimed mechanical properties, such as the bending modulus and modulus of rupture, on many lumber distributors' websites and the scientific literature. Ipe's bending modulus and modulus of rupture, as published by the Wood Handbook, are 20,100 MPa and 155,800 kPa, respectively (FPL 2010). Unfortunately, an extensive search revealed very little in regards to the mechanical properties of Ipe, specifically the stiffness elastic constants, C_{ij} . Wood is generally accepted as an orthotropic material; having three orthogonal axes in which the material properties differ as shown in Figure 1. For the purpose of this research, the three directions will be denoted as longitudinal (L), radial (R), and tangential (T). The longitudinal axis lies parallel to the fiber direction, the radial axis lies in the radial direction normal to the growth rings, and the tangential axis lies tangential to the growth rings.

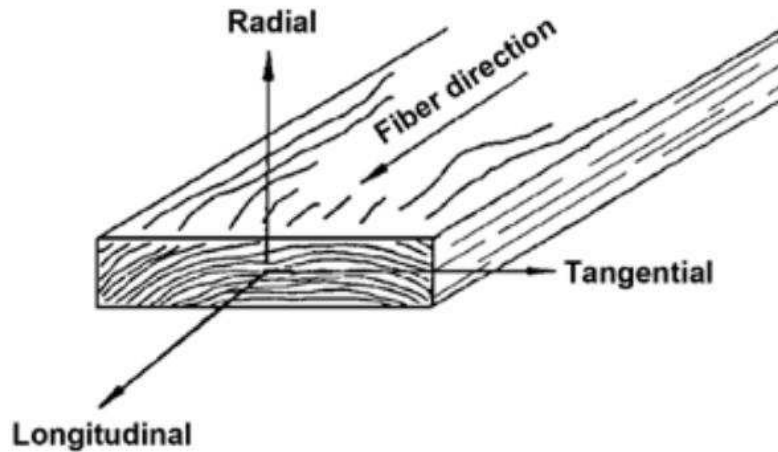


Figure 1 – (Source: Wood Handbook)

As an orthotropic material, wood consists of twelve elastic constants, nine of which are independent. From these constants, the compliance and stiffness matrices can be constructed that represent the overall relationship between the stress and strain exhibited within the material. The constitutive relationship between a material's strain state and its stress state is

$$\{\varepsilon\} = [S]\{\sigma\} \quad (1)$$

where [S] is the compliance matrix. The compliance matrix is a 6x6 matrix with 12 non-zero components and are functions of one or more of the following material properties: three principle moduli of elasticity (E_L , E_R , and E_T), three principle shear moduli (G_{RT} , G_{TL} , and G_{LR}), and six Poisson's ratios (ν_{LR} , ν_{RL} , ν_{RT} , ν_{TR} , ν_{TL} , and ν_{LT}) (FPL 2010). The compliance matrix is:

$$[S] = \begin{bmatrix} \frac{1}{E_L} & -\frac{\nu_{RL}}{E_R} & -\frac{\nu_{TL}}{E_T} & 0 & 0 & 0 \\ -\frac{\nu_{RL}}{E_R} & \frac{1}{E_R} & -\frac{\nu_{TR}}{E_T} & 0 & 0 & 0 \\ -\frac{\nu_{RL}}{E_R} & -\frac{\nu_{RL}}{E_R} & \frac{1}{E_T} & 0 & 0 & 0 \\ 0 & 0 & 0 & \frac{1}{G_{RT}} & 0 & 0 \\ 0 & 0 & 0 & 0 & \frac{1}{G_{TL}} & 0 \\ 0 & 0 & 0 & 0 & 0 & \frac{1}{G_{LR}} \end{bmatrix} \quad (2)$$

As mentioned earlier, one of the objectives of this research project is to determine these elastic constants through various methods. By inverting the compliance matrix, the stiffness matrix can be obtained to satisfy another constitutive relationship (Bodig 1993):

$$\{\sigma\} = [C]\{\varepsilon\} \quad (3)$$

$$\text{where } [C] = \begin{bmatrix} C_{11} & C_{12} & C_{13} & 0 & 0 & 0 \\ C_{21} & C_{22} & C_{23} & 0 & 0 & 0 \\ C_{31} & C_{32} & C_{33} & 0 & 0 & 0 \\ 0 & 0 & 0 & C_{44} & 0 & 0 \\ 0 & 0 & 0 & 0 & C_{55} & 0 \\ 0 & 0 & 0 & 0 & 0 & C_{66} \end{bmatrix} \quad (4)$$

$$C_{11} = \frac{1 - \nu_{23}\nu_{32}}{E_2 E_3 |S|} \quad (5)$$

$$C_{22} = \frac{1 - \nu_{31}\nu_{13}}{E_1 E_3 |S|} \quad (6)$$

$$C_{33} = \frac{1 - \nu_{21}\nu_{12}}{E_1 E_2 |S|} \quad (7)$$

$$C_{12} = C_{21} = \frac{\nu_{21} + \nu_{23}\nu_{31}}{E_2 E_3 |S|} \quad (8)$$

$$C_{13} = C_{31} = \frac{\nu_{31} + \nu_{21}\nu_{32}}{E_1 E_3 |S|} \quad (9)$$

$$C_{23} = C_{32} = \frac{\nu_{23} + \nu_{21}\nu_{13}}{E_1 E_2 |S|} \quad (10)$$

$$|S| = \frac{1}{E_1 E_2 E_3} (1 - 2\nu_{21}\nu_{32}\nu_{13} - \nu_{13}\nu_{31} - \nu_{23}\nu_{32} - \nu_{12}\nu_{21}) \quad (11)$$

There are many methods to obtain the elastic constants to construct the stiffness matrix. Generally, there are destructive and nondestructive methods. Destructive testing methods are used to obtain data on the material's behavior under various loads until failure. They typically result in more data and more understanding of the material. Nondestructive testing methods are, as the name implies, methods in which the material's composition isn't compromised. Loading a specimen within its elastic region, acoustics, and impact resonance, are all examples of nondestructive testing methods.

There are three common ways to load a specimen: tension, compression, and shear. When dealing with a unique material such as wood, tension and shear loading can prove to be difficult. Tension tests typically require a specific geometry and specialized grips for desired results and readings. Shear tests are "difficult if not impossible" due to the problem of applying pure shear to the specimen (Bodig 1993). As a result, ASTM 143 covers a number of standard tests including static bending and compression tests for small, clear specimens. Static bending is typically done to obtain the bending modulus of elasticity while the compression tests are to obtain the modulus of elasticity for a desired direction (parallel or perpendicular to the grain as denoted in the standard). Unfortunately, ASTM 143 does not cover tests specifically to obtain

all of the material's elastic constants. Thus, elasticity and mechanic theories will need to be utilized to obtain them.

A material's strain state can be expressed as a tensor, ε_{ij} . The strains in a new coordinate system can be denoted as ε'_{ij} , with the relationship between the two strain states expressed using the transformation matrix, A, as seen in Eq. 4 (Bodig 1993).

$$\varepsilon_{ij}' = A\varepsilon_{ij}A^T \quad (12)$$

$$\text{where } \varepsilon_{ij} = \begin{bmatrix} \frac{du_1}{dx_1} & \frac{1}{2}\left(\frac{du_1}{dx_2} + \frac{du_2}{dx_1}\right) & \frac{1}{2}\left(\frac{du_1}{dx_3} + \frac{du_3}{dx_1}\right) \\ \frac{1}{2}\left(\frac{du_2}{dx_1} + \frac{du_1}{dx_2}\right) & \frac{du_2}{dx_2} & \frac{1}{2}\left(\frac{du_2}{dx_3} + \frac{du_3}{dx_2}\right) \\ \frac{1}{2}\left(\frac{du_3}{dx_1} + \frac{du_1}{dx_3}\right) & \frac{1}{2}\left(\frac{du_3}{dx_2} + \frac{du_2}{dx_3}\right) & \frac{du_3}{dx_3} \end{bmatrix} \quad (13)$$

For any given stress state of a material, there is always a maximum and minimum normal stress that exists within a specific orientation. These normal stresses are called the principal stresses. Determining the orientation, the values of the principal stresses, and consequently the maximum shear stress, can be done via the principle of Mohr's Circle.

Obtaining the shear moduli requires some mechanics theory using strain transformation and Mohr's Circle. This process emulates the derivation by Aira et al (2014). With a specimen oriented 45 degrees from the longitudinal and radial axes, and assuming plane strain, the shear moduli can be derived to be:

$$G_{ij} = \frac{\tau_{ij}}{\gamma_{ij}} = \frac{\sigma_{j'}}{2(\varepsilon_{i'} - \varepsilon_{j'})} \quad (14)$$

2.2.2 Ipe

In the Wood Handbook, the Forest Products Laboratory (FPL), published a large mechanical property compilation of clear, straight-grained wood specimens (FPL 2010). The data for Ipe are listed in Table 1 for “green” moisture content. A “green” moisture content designation is treated as being well above the nominal 12% for optimal strengths. Only one elastic constant, the Modulus of Elasticity, was determined and published in this study. There are 9 total independent material properties to define the linear behavior of a material with the stiffness and compliance matrices. Thus, testing and analysis will need to be performed to obtain the other 8 independent elastic constants.

Table 1: Ipe Properties (FPL 2010)

Modulus of Rupture	155,800 kPa
Modulus of Elasticity	20,100 MPa
Work to Max Load	190 kJ m ⁻³
Compression Parallel to Grain	71,400 kPa
Side Hardness	13,600 N

From the Wood Handbook and Table 1, the Modulus of Elasticity (MOE) is referring to the bending modulus of elasticity. It is important to understand that the bending MOE is typically higher than the longitudinal elastic modulus by an average of 10% (FPL 2010). This behavior is a result of shearing deflection within the material. The modulus of rupture is a commonly accepted property in the industry to gauge its strength. Work to maximum load in bending reflects the specimen’s ability to resist shocks and is a measure of the combined strength and

toughness of the specimen in bending. The compressive strength parallel to grain refers to the maximum stress by a parallel-to-grain specimen with a ratio of length to least dimension of less than 11. The side hardness was a hardness test measured when the load is perpendicular to the grain.

As a material, wood can be highly variable when compared to other common materials. This is due to the many variables that affect wood, such as moisture content and density. Numerous studies have gone into how wood would behave under various environmental and loading conditions.

To determine the viability of Ipe in longitudinal barriers, its impact bending strength must be determined. Large-scale impact tests can be expensive to design compared to static bending, but several prediction measures have been proposed using simpler tests. Comparison between static bending and impact bending strengths in woods was studied by Leijten (2004). The purpose of Leijten's research was to determine any noticeable differences between the bending strengths extracted from static and impact loading tests. Bending tests were performed on 7 different species: Angelim Vermelho, Douglas Fir, Ash, Larch, and three heat treated or heat modified wood species. Leijten states that Larch and Ash were regarded as good shock absorbers. Out of the 7 species, only the Ash resulted in having an impact bending strength higher than the static bending strength. A FEM model was also built using Timoshenko-based elements. From the study, Ash and Douglas Fir were found to have no significant difference between the static and bending strengths, while the rest of the species showed significant differences from 40% to 60% reduction in strength from bending to impact strengths. The specimens that had a greater

reduction in bending strength were commercially graded where the lumber, under most design circumstances, would commonly have knots.

In another study done by Falk et. al, a larger sample was studied to determine wood characteristics after being in service for some time. Lumber was taken from deconstructed buildings at various sites. Sizes of 2x6, 2x8, and 2x10s were placed under static bending tests. A total of 1078 specimens were tested. Mean bending strengths dropped on an average of 25% while the mean stiffness increased on an average of 10% (Falk 2008). Another big conclusion from this study was that the failures tend to be correlated to the lumber's grade; the lower the lumber's grade increased its probability of failing. This implies that knots and other imperfections found in wood, as characteristic of lower grades, can greatly affect the material behavior.

2.2.3 Fiber Reinforced Polymers

Fiber reinforced polymer (FRP) products are becoming a versatile material for a variety of applications in the Civil and Structural engineering field (Gand 2013). FRP's practical structural applications have become steadily more popular due to the incredible ease of application and their inherit high strength-to-weight ratio. The most commonly used FRPs used in North America are carbon fiber reinforced polymers (CFRP) and glass fiber reinforced polymers (GFRP) (Gand 2013). FRP is a composite material consisting of a high strength fiber held in a matrix comprised of another material to maintain the dry fibers' configuration as well as to properly transfer the loads between the fibers. To obtain the most desirable performance out of

FRP, determination of the strength application, environmental conditions, and adhesion must be considered.

Usage of FRP to strengthen beams has increasingly become popular. Borri et. Al (2005) studied the use of FRP to reinforce old, pre-existing wood beams. Three major sets of beams were tested: un-reinforced, reinforced with CFRP, and reinforced with pre-stressed CFRP. Both sets of reinforced beams had the CFRP applied to the tensile face of the beam. Mechanical behaviors such as stiffness, ductility and more were analyzed through a series of four-point bending tests. Increases in flexural strength were measured up to 60.3% (Borri 2004). Tomasz et. al published a similar study eight years later with different applications. Six sets of reinforced beams were analyzed in this study, all of which have CFRP strips embedded within the cross section of the beam. Load capacities increased to as much as 79% (Tomasz 2012), showcasing the viability of FRP reinforcement.

To develop the correct load transfer between the FRP layer and the structural member, proper adhesion must be obtained through adhesives and surface preparation. Fyfe is one of the many manufacturers of FRP products. Their Research and Development department provided papers that highlighted FRP strength based on the wood preparation technique (Fyfe 2013). In the papers, Fyfe used three methods of preparation: alcohol wipe only (Group A), wire wheel followed by alcohol wipe (Group B), and grinding with a 4-grit angle grinder followed by alcohol wipe (Group C). They noted, “From observation, Group B (wire wheel) resulted in the greatest amount of roughening of the surface, showing visible scuff marks. Group C (40-grit sandpaper) smoothed the surface the most due to the high RPM of the angle grinder” (Fyfe

2013). Testing samples were constructed with a single 2"x10" wood panel, slightly protruding from two 7/16" oriented strand boards (OSBs) as seen in Figures 2 and 3. Adhesion between the wood panels and the OSBs were done with their Tyfo® BC bidirectional glass fabric along with their Tyfo® S Epoxy.



Figure 2: Wood Preparation Setup (Source: Fyfe)



Figure 3 – Wood Preparation Close-up (Source: Fyfe)

Average shear strengths at which failure occurred were calculated. Group A's, B's, and C's shear strengths at failure were 6098 lbf/ft, 5661 lbf/ft, and 5756 lbf/ft, retrospectively. The majority of the failures occurred in the delamination of the OSBs. All three preparation techniques performed near the same level of strength. Fyfe recommends to utilize a material surface preparation for the wood with the wire wheel at a minimum and notes that this "was performed on new wood materials and it is likely that bonding to aged materials will require more aggressive preparation than a simple alcohol wipe (Group A) to remove existing debris, oils, dirt, etc." (Fyfe 2013).

2.3 ROADSIDE BARRIERS

2.3.1 Introduction

Roadside barriers exist along roads, highways, and bridges with the primary purpose of roadside safety. These barriers vary in terms of the materials used and the configuration type. Concrete barriers, W-shape steel barriers, wood beams, and steel cables are common examples of longitudinal barriers that can be found. The American Association of State Highway and Transportation Officials (AASHTO) and the National Cooperative Highway Research Program (NCHRP) published guidelines and recommended procedures for the design and implementation of longitudinal barriers.

2.3.2 Testing and Criteria

Before construction of any type of longitudinal barrier, most of the barriers go through full-scale testing to satisfy a desirable test level given in NCHRP Report 350. EN-1317 is the European equivalent of this document, with the same purpose but with different classifications and criteria.

Within NCHRP Report 350, test levels range from 1 to 6 with increased levels of performance as the levels go upwards. Test level 3 is the minimum level at which most longitudinal barriers on which US highways are based. Each test level has its own impact conditions with various requirements to meet such a level. For example, to obtain NCHRP's test level 3, the longitudinal barriers must satisfy the following (as taken from NCHRP Report 350):

- Test barrier should contain and redirect the vehicle, without penetrating, underriding, or overriding the installation.
- Detached elements, fragments or other debris from the barrier should not penetrate or show potential for penetrating the occupant compartment, or present an undue hazard to other traffic, pedestrians, or personnel in a work zone.
- The vehicle should remain upright during and after collision although moderate roll, pitching and yawing are acceptable.
- The exit angle should be less than 60 percent of the entry angle.

The initial impact point of a vehicle should be taken at the critical impact points (CIPs) to account for the worst-case scenario (NCHRP 1993). For longitudinal barriers, there are two CIPs: “one that produces the greatest potential for vehicular pocketing or wheel snagging and one that produces the greatest loading on a critical part of the barrier, such as at a rail splice” (NCHRP 1993). NCHRP states that it is very possible for longitudinal barriers that both CIPs can coincide at the same location, resulting in one physical CIP to be analyzed.

The AASHTO Roadside Design Guide (2002) lists 21 common types of traffic barriers in use on America's roadways. Choosing the type of barrier is typically done on a case-to-case basis. For

example, the distance between the barrier and a terrain feature needs to be considered and compared to the deflection that each type of barrier would obtain upon impact. Thus, a desirable distance that is significantly smaller would require a more rigid barrier and a larger desirable distance would allow for more ductility in the barrier's properties. These allowable distances, or lateral deflections, separate roadside barriers into three (3) main categories: flexible, semi-rigid, and rigid.

An example of a flexible system would be the three-strand cable barrier (Figure 4). AASHTO contains specifications for three main types of three-strand cables. Cables are either 3 inches or 4 inches apart and are 2-3 feet above the ground. Testing resulted in lateral deflections from 7.8 feet to 11.5 feet. A TL-3 designation is given to the flexible three-strand cable system.

An example of a semi-rigid system would be the strong-post W-beam barrier (Figure 5). Railing consists of a steel sheet, roughly 3mm to 4mm in thickness, bent to a shape of a "W." There are variations in the specifications given by the AASHTO design guide. Posts can be either of W6x9 steel, 8 inch by 8 inch timber, or 6 inch by 8 inch timber. Systems using the steel posts have the TL-2 designation while the timber post systems have the TL-3 designation. A major advantage for the strong-post W-beam rail lies in its capability to remain functional after minor collisions (AASHTO 2002).

Concrete roadside barriers are an example of the rigid system (Figure 6). Geometries between the AASHTO specifications are very similar with two main parts: a wide base and a narrow

slope followed by a narrow upper part with a high slope. Heights range from 32 inches to 42 inches with no lateral deflections.



Figure 4: Flexible Barrier System: Three-Strand Cable (Source: blog.udot.utah.gov)



Figure 5: Semi-Rigid Barrier System: Strong Post W-Beam (Source: safety.fhwa.dot.gov)



Figure 6: Rigid Barrier System: Concrete (Source: safety.fhwa.dot.gov)

The Roadside Design Guide lists several standard barriers that utilize wood: the Ironwood Aesthetic Barrier, the Merritt Parkway Aesthetic Guardrail, and the Steel-Backed Timber Guardrail. All of these barriers are technically composites since they have a steel backing or support to assist with the required tension in the beam of the barrier. The Ironwood Barrier is a composite rail consisting of 8in diameter round posts with a 0.25in thick steel channel on the back end. The Merritt Parkway Aesthetic Guardrail utilizes 6in x 12in wood beams with 6in x 3/8in steel plates and splices. The Steel-Backed Timber Guardrail contains a 6in x 10in wood rail with a 3/8in thick steel plate.

Ultimately, the design of a roadside barrier can generally use any configuration as long as it satisfies NCHRP Report 350 test levels for the appropriate application. Material selection should

be based on considerations for reasonable sustainability, performance, and cost. Railing and post configuration selection should be based on desired performance along with the state of the surrounding terrain. Soil conditions should also be taken into account to gauge adequate anchorage for the barrier as a whole. Some other factors to consider, as listed by AASHTO, are life-cycle costs, maintenance, and aesthetics.

Development of barriers can prove to be a huge task. Thus, the NCHRP published the NCHRP Report 638: Guidelines for Guardrail Implementation to assist in that task. In this report, research was completed with the primary objective to develop guidelines for guardrails based on cost and performance. Models were used to determine encroachment probabilities along with a variety of scenarios that can be analyzed and placed into a benefit-to-cost analysis. Factors such as highway functional classes (e.g. freeway vs urban arterial), traffic volume, and terrain were included as a part of that analysis.

2.3.3 Rail Section Developments

Tabiei et al. (2000) researched possible rail section configuration using composite materials. Standard glass-reinforced, vinylester, pultruded shape “building blocks” were used to design eight (8) different beam configurations. Configurations primarily varied in the arrangement of the blocks. Quasi-static bending tests were then performed to determine general behavior, since it is generally indicative of their impact performance. Of the eight, four configurations were decided to take into the impact testing phase based on their performance. Tabiei et al. (2000) observed that the ultimate load decreased as the impact velocity increased but wasn’t able to determine the reasoning. Structural aspects were suggested as the cause rather than material

behavior. Beams that contained many “internal webs and individual cells” had better results in ultimate load resistance and duration of load.

Further research on composites was done by Bank et al (2001). In the study, they examined static and impact load resistances and responses for a multiple of roadside barrier configurations and was then compared to a standard, steel, semi-rigid, w-beam guardrail. Composite configurations covered a range of first and second generation arrangements. CGR10 from the second generation, as seen in Figure 7, was decided to have the closest behavior to that of the steel w-beam guardrail. Further testing was done via a 880-912 kg pendulum at impact velocities from 10 – 35 km/h (6.2 – 21.7 mph). Bank et al. (2001) concluded that the energy dissipation in the composite structure occurred due to the controlled tearing and separation of the rail and not from the elastic-plastic behavior of the material.



Figure 7: Cross-Section of “CGR10” Composite Configuration (Source: Bank 2001)

Dutta (2003) studied current guardrail implementation as a basis for an FRP composite based guardrail design. Fifteen guardrails were fabricated with profiles matching that of current, conventional guardrails. During testing, it was found that even when the FRP W-beam recovered to its original shape after the removal of the load, the W-beam sustained significant local damage. For energy absorption, the FRP was not able to perform as well as the conventional steel W-beams. This can be alleviated with arrangements to take advantage of the FRP

properties. Dutta (2003) stated that progressive crushing via "extensive microfracturing of the matrix and partial failure of the fibers" was the main objective in the design to obtain a large amount of energy absorption.

Efforts have been made to develop longitudinal barriers using wood as a material that would mimic the performance of steel W-beam guardrails while remaining cost-effective. Davids et al. (2006) made one of these efforts by implementing common low-grade lumber found in the United States. A major drawback for using wood lies in the strength to weight ratio. Steel W-beams' strength to weight ratio is nearly twice as high than common wood beams making them more appealing for use in transporting and construction. Davids et al. (2006) compensated for this drawback by proposing the use of fiber-reinforced polymer (FRP) on the back/tensile side of a beam. The additional tensile strength along with the low weight of FRP allows for less wood material to be utilized to obtain the same strength properties. In the study, the rail cross-section consists of a "brickwork layup from readily available mixed hardwoods (primarily red maple)...reinforced with a 3.5-mm thick, unidirectional E-glass FRP, which serves both as a tension ribbon and as flexural tension reinforcement during vehicle impact" (Davids 2006). The red maple's elastic modulus was noted as 11.3 GPa (1640 ksi) at 12% moisture content and a modulus of rupture of 92 MPa (13 ksi) while the E-glass FRP's elastic modulus was noted as 40 GPa (5800 ksi).

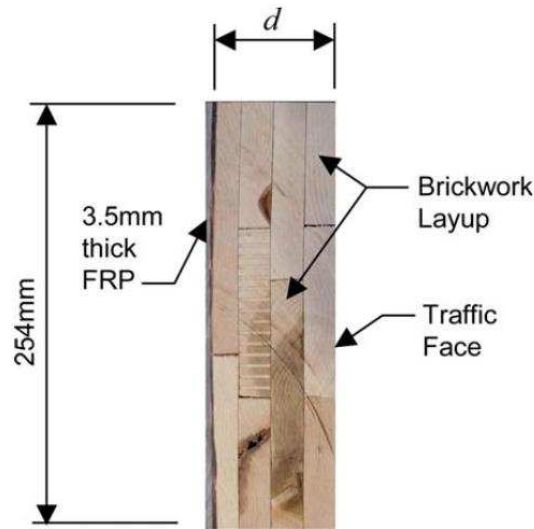


Figure 8: Wood/FRP Composite Cross-Section Developed by Davids et al. (Davids 2006)

Analysis of the rail cross-section with varying widths was performed via Barrier VII, a commonly used 2D dynamic finite element program to evaluate guardrail performance. Overall, good results were obtained when comparing to those of a steel W-beam rail. It was found that the thinner the cross-section, the better performance was obtained. This phenomenon was attributed to the higher ratio of FRP to lumber. Davids et al. (2006) felt confident that this rail cross-section “has a high probability of passing a TL-3 crash test.” A follow up to a TL-3 crash test could not be found in the literature.

2.4 MODELING OF RAILS AND BARRIERS

2.4.1 Modelling Techniques

Numerous techniques have been utilized to numerically model and analysis roadside barrier systems. These include BARRIER VII, LS-DYNA, and a multitude of finite element method analysis tools.

BARRIER VII was developed by Powell, G.H., and published by the University of California, Berkeley. It is a simulation code that “utilizes two-dimensional structural finite elements to model physical rail components such as railings, posts, cables, hinges, etc. and utilizes two-dimensional, three degree-of-freedom planar vehicle models” (FHWA 1998). The advantages of BARRIER VII have been to pinpoint CIPs in roadside barriers easily (AASHTO 2009). Unfortunately, due to the two-dimensional nature of the simulation, vehicular response and stability cannot be predicted.

Another numerical analysis tool is LS-DYNA and is widely used in analyzing roadside barriers. Produced by Livermore Software Technology Corporation, LS-DYNA is a finite element analysis (FEA) code. FEA is a general solution method that is used in a wide range of fields due to its accuracy by linking small “finite” elements and modelling their contact behavior and responses under specified boundary conditions. LS-DYNA, as an FEA method, has “great flexibility in being able to model widely varying impact situations ranging from vehicle-barrier interaction (e.g. prediction of snagging and vaulting), vehicle dynamics (e.g. stability and trajectories), and assorted impact conditions (e.g. tracking, side, and general non-tracking)” (FHWA 1998). It is also important to note that the FEA method can potentially save a lot of money from the resources required for a full-scale test. Some disadvantages for using LS-DYNA lies in the time to “develop and validate” models. Also, due to its detailed accuracy, running a model can be computationally demanding, sometimes requiring robust computer hardware for reasonable computational times.

Abaqus is a FEA software package that has been used for roadside barrier analysis. Abaqus is an extremely robust FEA package which is developed and maintained by SIMULIA. As a complete FEA package, Abaqus offers a wide range of finite element types, various linear and nonlinear analysis methods, a multitude of material definitions, numerous element interaction modes, and more. The full ABAQUS suite consists of 6 components: Abaqus/CAE, Abaqus/Standard, Abaqus/Explicit, Abaqus/CFD, Abaqus Multiphysics, and Add-on Tools. For roadside barriers, Abaqus/Explicit is used to analyze roadside barrier behavior during a vehicular impact. This component is primarily used to study “brief dynamic events such as consumer electronics drop testing, automotive crashworthiness, and ballistic impact” (SIMULIA 2015).

2.4.2 Experiments and Models

To validate numerical models, a full-scale experiment is typically performed or data from a previously full-scale experiment is gathered to compare results. This section will cover various experiments and models that have been performed in the roadside barrier field. Tests of this magnitude are beyond the scope of the present study.

Thiele et al.(2011) utilized the BARRIER VII computer code to aid in their development of a low-cost, energy-absorbing bridge rail. Three S3 x 5.7 (S76 x 8.5) and two W6 x 8.5 (W152 x 12.6) post models were created based on previously performed and published tests based on the Midwest Guardrail System (MGS). Geometry and material properties of the guardrail were modelled based on a standard 12-gauge (2.66 mm) corrugated guardrail. With two vehicle models on top of all that, a series of full barrier models were created to extract maximum lateral deflections and pocketing angles for the rail design. “For each post post model, barrier

deflections were found to be quite similar to those observed in the MGS crash testing program, and pocketing angles were well below recommended limits” (Thiele 2011). Thus, by using BARRIER VII, the CIPs of the barrier system were able to be pinpointed for proper analysis. It is important to note that the behavior of the vehicle during the simulation wasn’t studied, since BARRIER VII does not have the capabilities to do so, nor was it within the scope of the study.

Whitworth et al. (2004) studied the crashworthiness of a modified W-beam guardrail design using the LS-DYNA modelling and analysis tool. Analysis is based on and compared to a test performed by the Midwest Roadside Safety Facility on a modified “G4-1S” W-beam guardrail. Patran, a popular pre/post-processing software for FEA, was used to create the model’s geometry and define the finite elements. A multitude of material behaviors were defined to capture the varied elastic and piecewise linear elastic plastic nature of the barrier system. Post and rails were modeled with quadrilateral shell elements while the wooden blockouts used eight node reduced integration hexahedral solid elements. To model the soil in which the posts are in place, a cylindrical block using eight node hexahedral solid elements were placed around each post. Vehicle used was a model of a Chevrolet C2500 pickup truck. Whitworth et al. (2004) found that the model created was in acceptable agreement with the test performed by the Midwest Roadside Safety Facility. In other words, the study was able to simulate an impact scenario within LS-DYNA.

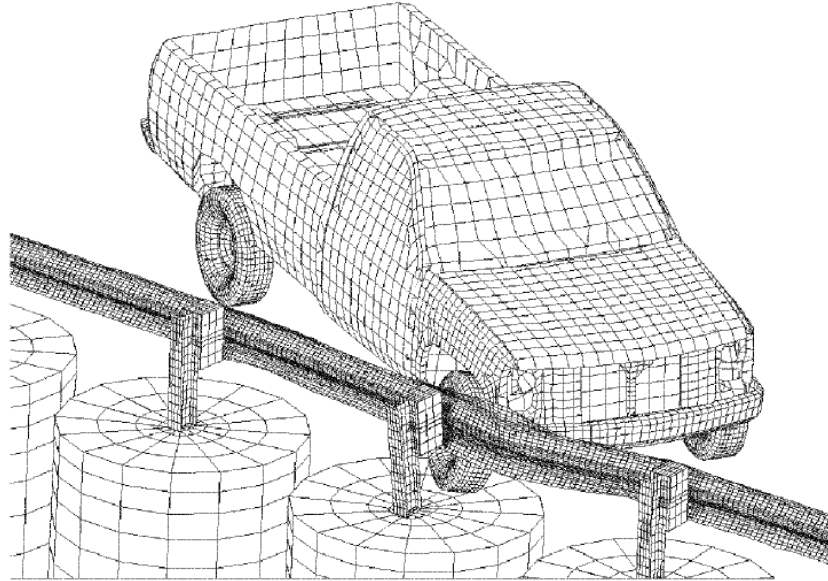


Figure 9: FEA Model of “G4-1S” W-beam guardrail with LS-DYNA (Whitworth 2004)

Another study that utilized LS-DYNA involved a more unique barrier configuration, and consequently, more complex. Thiyahuddin et al. (2014) performed 5 full-scale experimental tests on a regular portable water-filled road safety barrier (PWFB) system, and a retrofitted PWFB system. Regular PWFB barriers comprises of a hollow shell made up of Medium-Density Polyethylene (MDPE) designed to hold a recommended amount of 200 kg (~440 lbs) of water. Retrofitted PWFB barriers build on the regular configuration, adding an “inner steel endoskeleton and outer Polyurethane foam cladding”, while still designed to hold the same volume of water (Thiyahuddin 2014). A design schematic published along with the study can be seen in Figure 10. A horizontal impact test rig that accelerates along rails was used to strike the PWFB systems while a camera captures 1000 frames per second over 4 seconds. Due to difficulties in attaching instrumentation to the barrier, a “motion-based method to extract kinematic data” was used. Once the experimental tests were performed, a complex finite element numerical model was then developed using LS-Dyna. Due to the unique arrangement and composite nature of the PWFBs, several modelling techniques were used. The various

material definitions like elastic plastic, and piecewise linear plasticity were defined. Belytschko-Tsay single integration-point shell elements were used for the outer shell while Smoothed Particles Hydrodynamics (SPH), a computational Lagrangian hydrodynamic particle method, was used to model the water particles. Ultimately, Thiyahuddin et al. (2014), was able to produce numerical results with LS-DYNA that were agreeable with the experimental results.

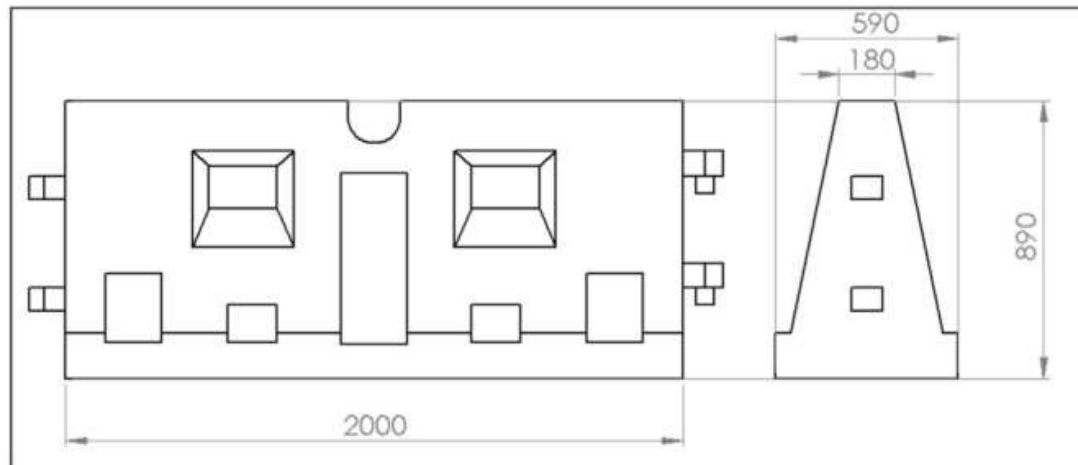


Figure 10: Portable Water-Filled Road Safety Barrier Schematic (Thiyahuddin 2014)

Shen et al. (2008) used Abaqus/Explicit 6.5 to simulate typical guardrail impact scenarios in 2008. The purpose of the study was “to verify the crashworthiness of a given design of guardrail system, and optimize the relative vertical distance between centroid of vehicle and mounting height of (the) W-beam” (Shen 2008). A 1,500-kg car was modelled to strike the guardrail at 80 km/h with the car direction 20° offset from the guardrail direction. Four-point shell elements were used for the W-beam, posts, and offset blocks while the vehicle utilized 3-dimensional solid elements. The model resulted in a proper redirection of the car, verifying the crashworthiness of the guardrail system. The trajectory and redirection of the vehicle by the guardrail agreed with published experimental data. Further analysis went into this study by determining the height in which the maximum amount of absorbed energy was obtained. Once the height was determined, a 10,000-kg truck was then modelled to strike the same guardrail configuration at the same angle

of approach, but with a velocity of 40 km/h rather than the car's 80 km/h. Models were not compared to any experimental data, but was mainly used to assess the height difference between the vehicle and barrier where the most energy was absorbed.

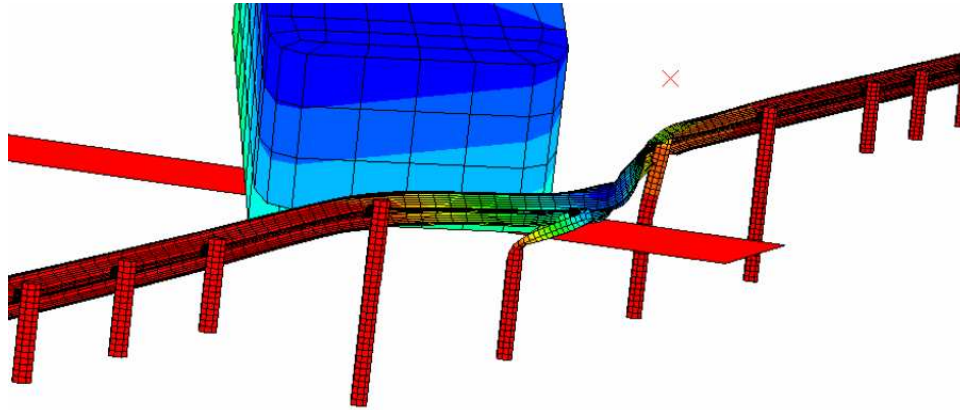


Figure 11: Post-Processing Analysis via Abaqus (Shen 2008)

CHAPTER 3 - METHODOLOGIES AND RESULTS

3.1 INTRODUCTION

The study of Ipe and its viability in roadside barriers falls into two main parts. First, material testing is needed to obtain all 9 independent elastic constants and to assess its stiffness with and without CFRP. This will result in a full stiffness matrix that will capture the mechanic behavior of the material. Secondly, impact models were used to compare various configurations of barriers using Ipe to that of the commonly used barrier today, the steel W-beam.

3.2 MATERIAL TESTING

To obtain the elastic constants required to understand the behavior of Ipe, a series of tests were performed. The following sections detail these tests.

3.2.1 Samples

Based on availability and limited funding, thirty six (36) 38.1-mm by 38.1-mm samples, each approximately 0.610 meters in length, were acquired from a local supplier. The specimens were only treated at the endpoints to prevent environmental contamination while in storage. Each specimen was thus labelled 1 through 36. Ipe was tested primarily under a moisture content of 4.5%. Compression testing also utilized a humidior to increase the moisture content (MC) to 8.0%. Densities under 4.5% MC and 8.0% MC were $1,001 \text{ kg/m}^3$ and $1,035 \text{ kg/m}^3$, respectively.

3.2.2 Static three-point bending

The first test that was performed was a static three-point bending test. The bending test is one of the most common tests to assess a wood's strength and stiffness (FPL 2010). For three-point bending, ASTM provided guidelines within ASTM 143 for 2-inch by 2-inch (50.8-mm by 50.8-mm) and 1-inch by 1-inch (25.4-mm by 25.4-mm) cross-sections for small clear wood specimens. A 2-inch by 2-inch specimen would require a span of 30 inches (0.762 meters) while a 1-inch by 1-inch cross-section would require a span of 16 inches (0.406 meters). Based on this, it was decided to use a span of 0.508 meters (20 inches) for the 38.1-mm by 38.1-mm samples.

An Instron Universal Testing Machine (UTM) was used to apply the loading with a 4.45-kN (5-lb) load cell while the specimens were held in place as seen in Fig. 12. Three specimens were taken to complete failure. The remaining 33 specimens were then loaded within approximately two-thirds of the observed proportional limit of the failed specimens. Load vs displacement data was extracted during this testing process.



Figure 12: Instron UTM with Loading Mechanism and Ipe Specimen

A load versus deflection plot from the initial destructive three-point bending tests can be seen in Figure 13. From the plots, all three specimens had fairly similar elastic moduli. The behavior of the specimens start to differ once their proportional limits have been reached. The first specimen initially failed at 14.97kN at 13.42mm, the second at 10.96kN at 9.78mm, and the third at 19.09kN at 17.13mm. This equates to a bending stresses of 206 MPa, 151 MPa, and 335 MPa. A summary of these results can be seen in Table 2. Instead of complete material failure, the specimens would continue to resist the load. The length at which the specimen would resist the load varied from each other. This implies that the ductility in Ipe has a significant uncertainty. As the Ipe specimen continues to resist the load, the more energy it is absorbing. Total energy absorbed were 237.72 J, 87.76 J, and 335.15 J for specimens 1, 2, and 3, respectively.

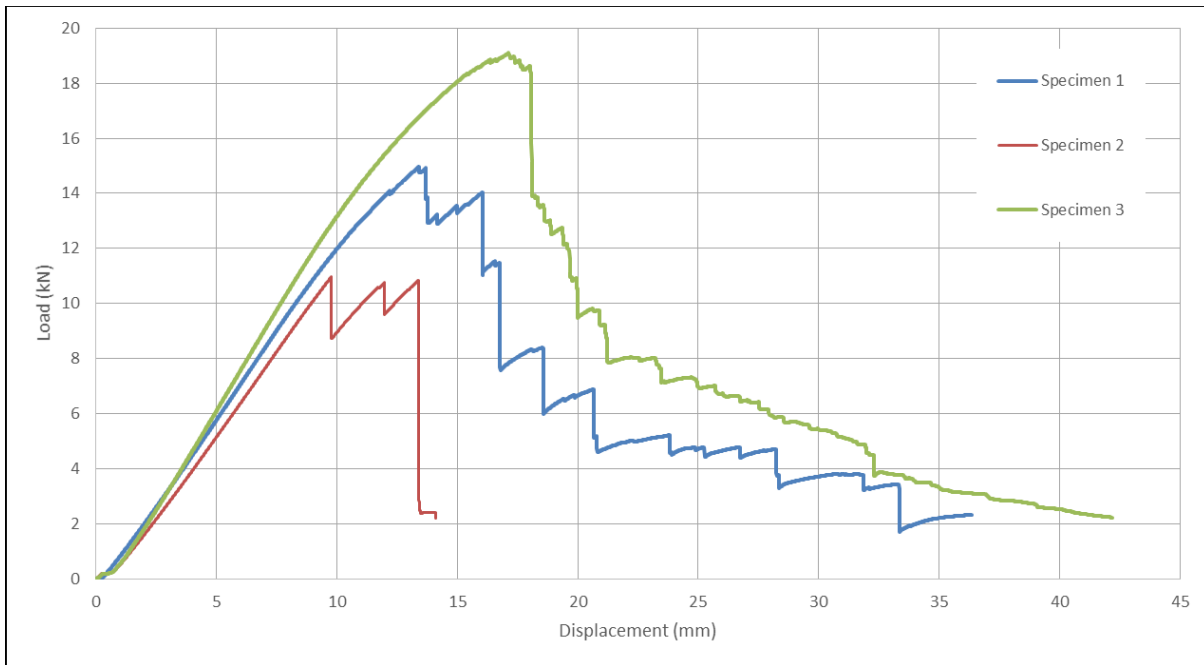


Figure 13: Load vs Displacement at Midspan



Figure 14: Ipe 3-pt Bending Specimens. (1 on top, 3 on bottom)

From the initial bending tests, it was decided to load the remaining specimens at midspan to 8.90 kN to stay within the elastic limit. Results are shown in Table 2. Based on elementary beam theory, the mean bending modulus of elasticity was 17.93 GPa with a standard deviation of 1.17 MPa and the mean midspan deflection was 7.72 mm with a standard deviation of 0.51 mm. To compare, the Wood Handbook’s published bending modulus of elasticity was 20.13 GPa. Difference between the values is likely due to the difference in moisture content. The tested specimens within the study were at 4.5% moisture content while the Wood Handbook’s were of green moisture content.

Table 2: Three-Point Bending Results for Ipe Specimens

Destructive Results	1	2	3
At Initial Failure			
Load (kN)	14.97	10.96	19.09
Midspan Disp. (mm)	13.42	9.78	17.13
Energy Absorbed (J)	237.72	87.76	335.15

Non-Destructive Results	Mean	Standard Deviation	Wood Handbook	Theoretical
MOE (GPa)	17.93	1.17	20.13	-
Deflection (mm)	7.72	0.51	-	6.88

3.2.3 Static three-point bending with CFRP

Three specimens were retrofitted with Carbon Fiber Reinforced Polymer (CFRP) sheets. A unidirectional carbon fabric product names “Tyfo® SCH-41 Composite” was used along with “Tyfo® Epoxy.” Both products were developed by Fyfe, a company that specializes in various FRP products. Table 3 lists the dry fiber properties along with the epoxy material properties as published on their datasheets.

Table 3: Dry Fiber and Epoxy Material Properties

	Dry Fiber Properties	Epoxy Material Properties
Tensile Strength	4.0 GPa (580,000 psi)	72.4 MPa (10,500 psi)
Tensile Modulus	230 GPa (33.4 x 10 ⁶ psi)	3.18 GPa (461,000 psi)
Ultimate Elongation	1.7%	-
Density	1.74 g/cm ³ (0.063 lbs/in ³)	-
Elongation Percent	-	5.0%
Flexural Strength	-	123.4 MPa (17,900 psi)
Flexural Modulus	-	3.12 GPa (452,000 psi)

Table 4: FRP Composite Laminate Properties

	Typical Test Value	Design Value
Ultimate Tensile Strength (Primary direction)	986 MPa (143,000 psi)	834 MPa (121,000 psi)
Elongation at Break	1.0%	0.85%
Tensile Modulus	95.8 GPa (13.9 x 10 ⁶ psi)	82 GPa (11.9 x 10 ⁶ psi)
Flexural Strength	123.4 MPa (17,900 psi)	104.8 MPa (15,200 psi)
Flexural Modulus	3.12 GPa (452,000 psi)	2.65 GPa (384,200 psi)
Nominal Laminate Thickness	1.0 mm (0.04 in)	

Application of Fyfe’s CFRP products is dependent on the material(s) in which the FRP is being applied to as well as environmental conditions to which the final composite will be exposed. Fyfe’s R&D department provided two research papers on the shear transfer and direct pull off using different application processes, as discussed in the literature review section. Based on their studies, preparation by solely an alcohol wipe provided the highest strength for wood.

The three beam specimens were initially wiped with alcohol on the tensile face. The Tyfo® S Epoxy was then applied to the same face. Dry fibers, while remaining taut, were then laid down within the epoxy. Using tape to keep the dry fibers taut, the specimens were left to cure for 7 days at room temperature. This curing method was done to mimic the 7-day curing that Fyfe performed in their studies. Product test and design property values of the overall composite, as published on the product page, can be found in Table 4. Static three-point bending of the three specimens was then performed via the same measure as the previous three-point bending tests.

Midspan deflections are shown in Table 5. Application of the CFRP layer resulted in only a 17% increase in stiffness with a deflection of 6.3mm. A transformed analysis showed that the bending elastic modulus of the new composite section is approximately 61.32 GPa. This

increase in stiffness does not reflect the high percentage increase of strength seen in previous studies (up to 79%), several factors are suspected. The primary suspect is the relative difference in stiffness between the wood and the CFRP. In the studies performed by Borri et. al (2008) and Nowak et. Al (2013), old commonly used structural lumber, such as pine-wood, were studied. Structural lumber is typically only a third or half of the stiffness of Ipe. Thus, when applying FRP in various ways to increase their stiffness, the percentage increase would be more significant. Another suspect would be the type of application, specifically with the study performed by Tomasz et. al. In that study, a 79% increase was from a specimen in which the FRP sheets were placed within the cross-section, rather than being adhered to the tension face. This allowed for an increase in flexural stiffness from normal bending stresses along with shear stresses. With only an increase of 17%, using CFRP does not appear to be worth the cost.

Table 5: Three-Point Bending for Ipe with CFRP Specimens

	Specimen #1	Specimen #2	Specimen #3	Mean
Midspan Deflection @ 8.9 kN (mm)	6.32	6.22	6.32	6.30

3.2.4 Compression Tests

Nondestructive compression tests were performed as another way to obtain the material’s elastic constants. Six (6) specimens total were milled out for this test with the orientations as shown in Figures 15 and 16. Specimen dimensions are given in Table 6 with the specific material properties in which each specimen is being tested for. The first three test specimens were milled to orient in each of the three primary material directions, with strain gauges installed and oriented in those same three directions. Three additional specimens were oriented at 45 degrees about each of the primary axes with strain gauges installed and oriented with the direction of

loading and the direction orthogonal to the loading axis and the axis about which the sample is rotated. These configurations allow the determination of the shear moduli using standard stress and strain transformations.

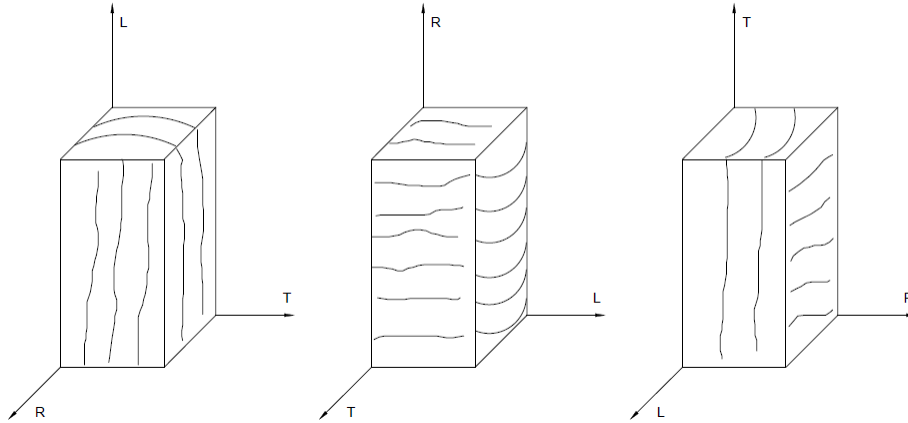


Figure 15: Compression Test Sample Orientations – 1

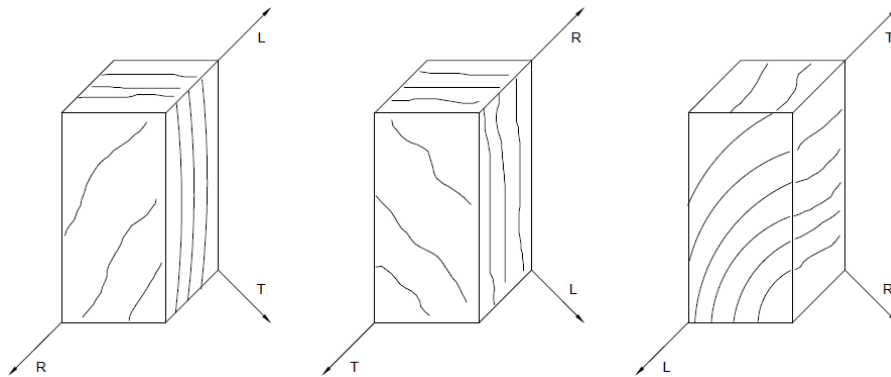


Figure 16: Compression Test Sample Orientations – 2

Table 6: Mean dimensions of test specimens

Direction of Loading	Dimensions (mm)	Properties
Longitudinal (Fig. 1)	38.10x38.10x150.5	E_L, ν_{LR}
Radial (Fig. 1)	37.08x32.89x38.10	E_R, ν_{RT}
Tangential (Fig. 1)	38.25x33.71x37.29	E_T, ν_{LT}
LT Plane (Fig. 2)	13.28x14.40x26.92	G_{TL}
LR Plane (Fig. 2)	16.43x16.51x26.90	G_{LR}
RT Plane (Fig. 2)	14.25x16.51x29.34	G_{RT}

Loading was performed with the Instron UTM. Load data was extracted via the load cell while the strain data were all fed through a strain indicator. Loadings on all samples were performed at a rate of 0.127 mm per minute and repeated multiple times to ensure consistency. Tests were performed at moisture contents of 4.5% and 8.0%. Densities of the 4.5% and 8.0% specimens were $1,001 \text{ kg/m}^3$ and $1,035 \text{ kg/m}^3$, respectively. All 3 elastic moduli E_L , E_R , and E_T were then obtained from the slope of the best-fit line off of the stress versus strain data (Figures 17 – 19). The values for Poisson ratio were obtained from the best-fit line off of the strain vs strain data. The shear moduli were calculated using the derivation by Aira et al. (2014).

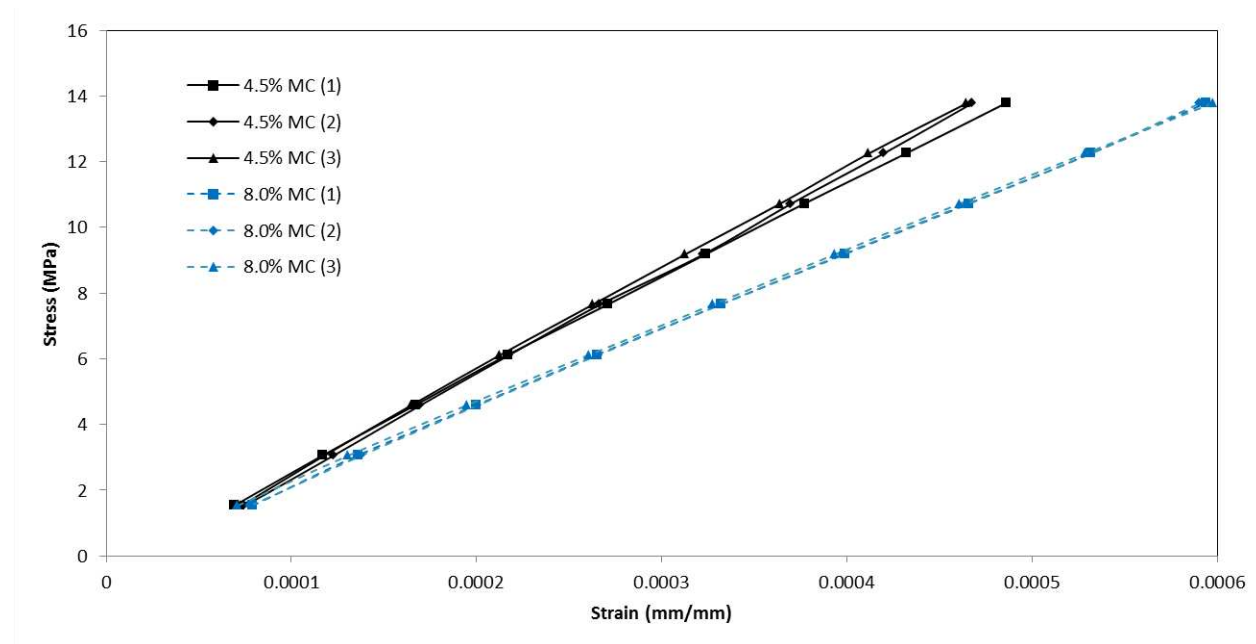


Figure 17: Longitudinal Stress vs Strain

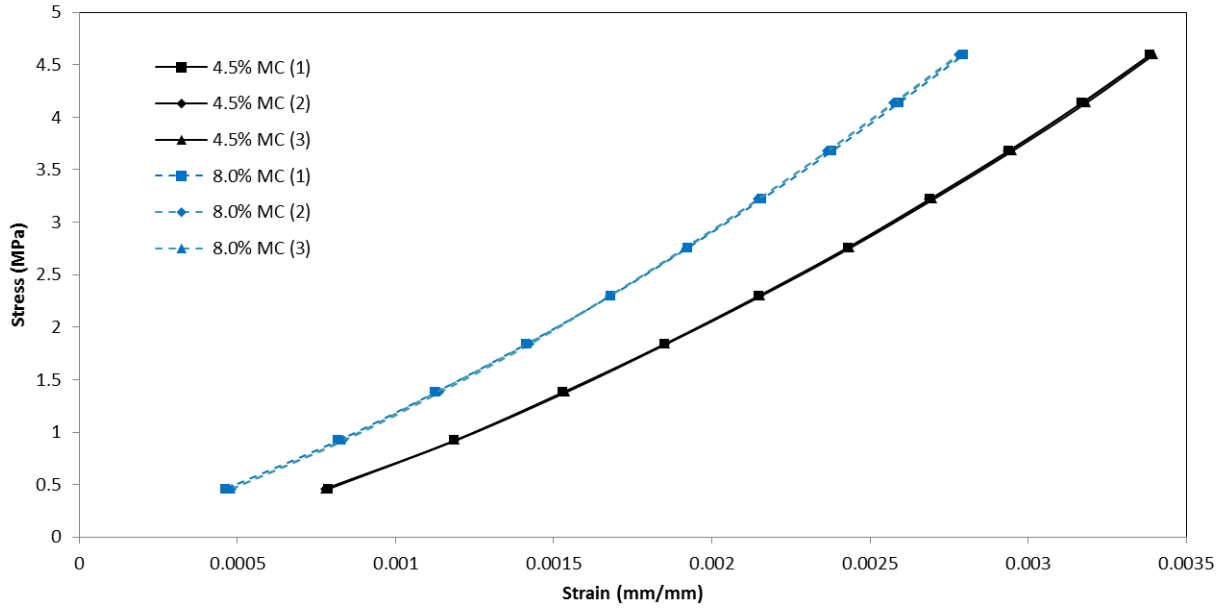


Figure 18: Radial Stress vs. Strain

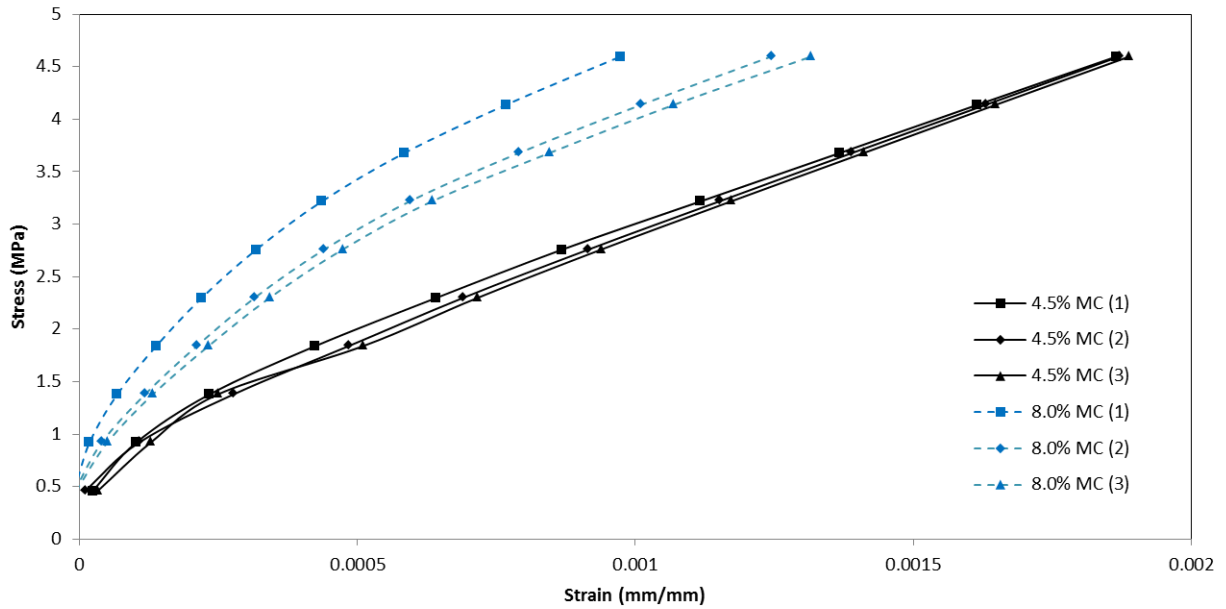


Figure 19: Tangential Stress vs. Strain

Longitudinal stress versus longitudinal strain can be seen in Figure 17 and remained linear throughout the loading period. Stress versus strain for both the Radial (Figure 18) and Tangential (Figure 19) had a curved behavior at the initial phase of the loading and became

linear for the majority of the loading period. Moduli were calculated within that linear range. In the case of the Radial loading, initial resistance was weak (shallow slope) and became stronger (steeper slope) as the loading period continued. The opposite was true for the Tangential loading: initial resistance was strong (steeper slope) and became weaker (shallow slope) as the loading period continued. There could be many reasons for this type of behavior, but that is beyond the scope of this study.

Results of the material properties from the compression tests for both moisture contents are shown in Table 7. E_L was calculated to be 30.4 GPa at 4.5% MC and 23.4 GPa at 8.0% MC with a drop in the strongest elastic modulus of 23.1% with an increase of 3.5% in moisture content. E_R and E_T both saw an increase from 4.5% MC to 8.0% MC of 13.3% and 14.1%, respectively. All shear moduli dropped from the increase with G_{RT} , G_{TL} , and G_{LR} seeing a decrease of 12.6%, 4.6%, and 1.4%, respectively. All Poisson ratios stayed relatively the same with very slight increases ranging from 1.2% to 4.9%. From here, the stiffness matrix can finally be created. For 4.5% MC and 8.0% MC, the stiffness matrices are shown in Eq. 15 and Eq. 16.

Table 7: Material Property Results from Compression Tests

Property	@ 4.5% MC (GPa)	@ 8.0% MC (GPa)	% difference
E_L	30.4 +/- 1.04	23.4 +/- 0.22	-23.1%
E_R	1.59 +/- 0.01	1.80 +/- 0.02	13.3%
E_T	1.95 +/- 0.04	2.23 +/- 0.28	14.1%
G_{RT}	0.98 +/- 0.01	0.97 +/- 0.00	-12.6%
G_{TL}	1.34 +/- 0.01	1.28 +/- 0.01	-4.6%
G_{LR}	6.82 +/- 0.03	5.96 +/- 0.15	-1.4%
ν_{LR}	0.550	0.557	1.2%
ν_{LT}	0.587	0.603	2.7%
ν_{RT}	0.477	0.500	4.9%

$$[C]_{4.5} = \begin{bmatrix} 32.4 & 1.95 & 1.56 & 0 & 0 & 0 \\ 1.54 & 20.0 & 7.50 & 0 & 0 & 0 \\ 2.12 & 12.5 & 24.5 & 0 & 0 & 0 \\ 0 & 0 & 0 & 0.98 & 0 & 0 \\ 0 & 0 & 0 & 0 & 1.34 & 0 \\ 0 & 0 & 0 & 0 & 0 & 6.82 \end{bmatrix} \text{ N/m}^2 \quad (15)$$

$$[C]_{8.0} = \begin{bmatrix} 25.0 & 1.54 & 12.2 & 0 & 0 & 0 \\ 1.80 & 23.0 & 8.60 & 0 & 0 & 0 \\ 2.55 & 15.1 & 28.3 & 0 & 0 & 0 \\ 0 & 0 & 0 & 0.97 & 0 & 0 \\ 0 & 0 & 0 & 0 & 1.28 & 0 \\ 0 & 0 & 0 & 0 & 0 & 5.96 \end{bmatrix} \text{ N/m}^2 \quad (16)$$

Comparisons of the 8.0% MC tests are shown along some of the most popular structural lumber in North America in Table 8. Ipe at 8.0% MC is shown to be stiffer in all areas except for E_R , with E_L and G_{LR} having the largest differences.

Table 8: Material Property Results Comparison to Common NA Woods (FPL 2010)

	Ipe (4% MC)	Oak (Northern Red, 12% MC)	Maple (Red, 12% MC)	Pine (Loblolly, 12% MC)
E_L (ksi)	30.4	12.5	11.3	12.3
E_R (ksi)	1.59	1.93	1.58	0.96
E_T (ksi)	1.95	1.03	0.76	1.39
G_{RT} (ksi)	0.98	-	-	0.16
G_{TL} (ksi)	1.34	1.01	0.84	1.00
G_{LR} (ksi)	6.82	1.11	1.50	1.01

3.2.5 Impact Resonance Testing

Another method to obtain material properties of Ipe would be to analyze its natural frequencies under various excitations. ASTM E1876 outlines standardized methods for this type of testing, though it is specifically for elastic, homogeneous, and isotropic materials. Also, ASTM E1876

has specific guidelines for material sizes resulting in their material property calculations to be relatively specific to those guidelines.

Impact Resonance testing was done with a Grindosonic, which is designed to detect frequencies through a sensitive microphone. A total of 9 beam specimens were milled with average dimensions shown in Table 9. Three beam specimens had their spans in the longitudinal direction, three in the radial direction, and three in the tangential direction. A small impact apparatus with a small metal bearing was used to excite various vibrational modes. Frequency readings were fairly inconsistent and could be attributed to the location of impact with the apparatus onto the specimens and the material itself. Consequently, impact resonance testing was not able to produce usable results.

Table 9: Dimensions of Impact Resonance Specimens

Direction of Span	Tangential			Radial			Longitudinal		
Specimen No.	1	2	3	1	2	3	1	2	3
mass (g)	1.756	1.68	1.81	1.75	1.57	1.06	887	925	887
width (mm)	11.13	10.58	10.81	12.01	10.72	10.1	38.1	38.1	38.1
length (mm)	37.42	37.51	37.22	37.85	37.84	29.89	609	635	609
thickness (mm)	4.2	4.21	4.48	3.83	3.85	3.5	38.1	38.1	38.1

3.2.6 Resonant Ultrasound Spectroscopy

Resonant Ultrasound Spectroscopy (RUS) was also explored to obtain material properties of Ipe. RUS involves inducing vibrations over a range of frequencies within a sample. Using an oscilloscope and computer software, natural frequencies are recorded by a local RUS expert and used to calculate the material properties. Figures 20 and 21 are snapshots of the spectrum from the induced vibrations. Peaks are not clearly defined and tend to be fairly broad. This behavior existed for two specimens: one with dimensions of 38 mm x 34 mm x 41 mm and the other with

dimensions of 7 mm x 10 mm x 35 mm. Figures 20 and 21 are from the second, smaller specimen. Clear peaks are expected, as can be seen by the work done by Longo et al. (2012) to calculate material properties for a beech wood sample (Figure 22). The broad peaks means that the internal damping are fairly large. Consequently, due to the lack of clear peaks, RUS was not able to produce usable results.

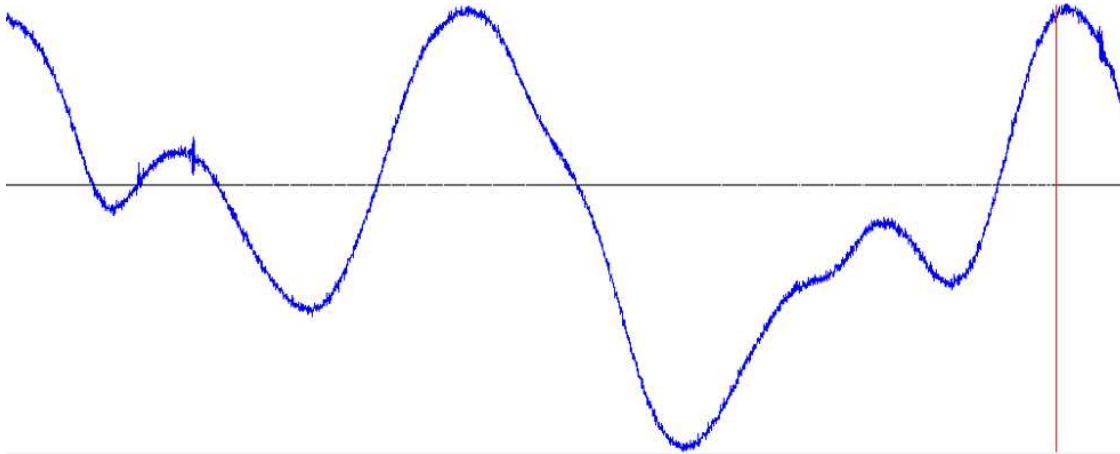


Figure 20: RUS Analysis between 130 Hz and 170 Hz

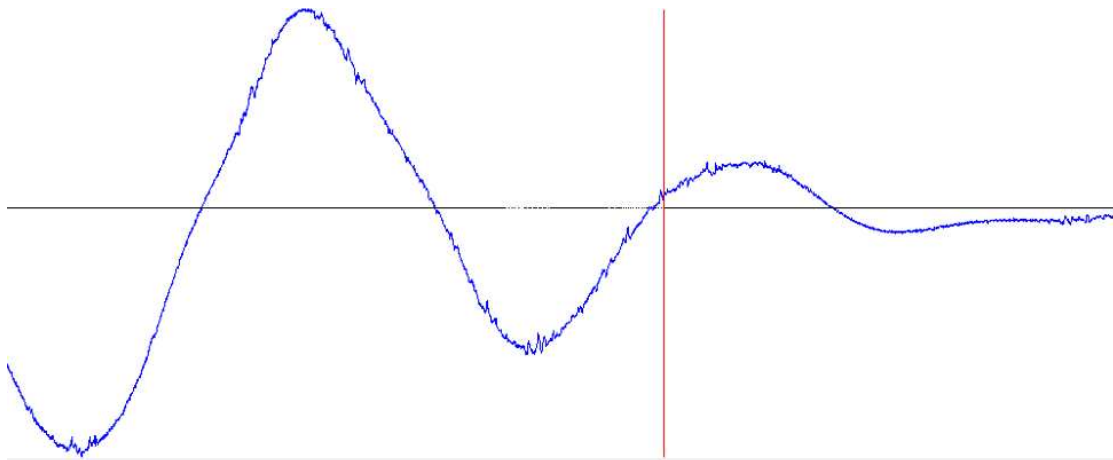


Figure 21: RUS Analysis between 200 Hz and 240 Hz

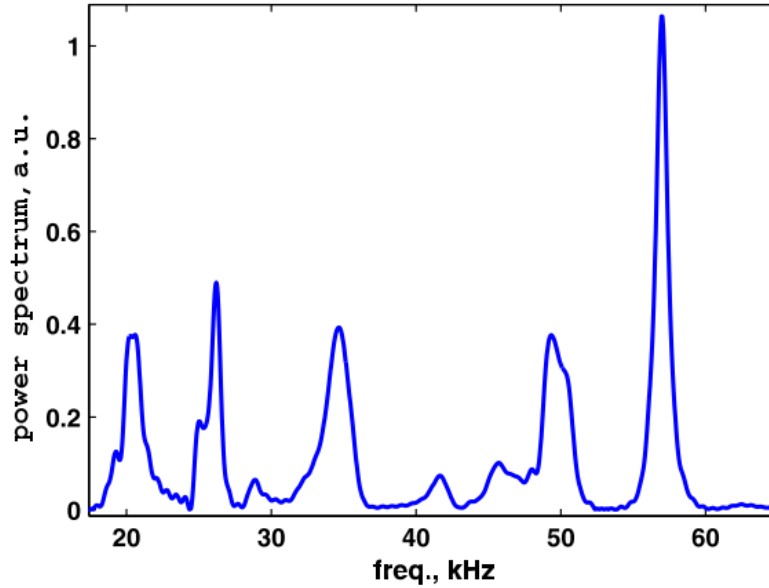


Figure 22: RUS Analysis of Beech Sample as published by Longo et al. (2012)

3.2.5 Validation

To verify the calculated material properties of Ipe, a finite element analysis was used to simulate the 3-point bending tests that were performed as part of this study. Using Abaqus CAE, two models were created to double check convergence of the results: one coarse and one fine. The coarse beam model consisted of 6,633 nodes with 4,900 elements. The fine beam model consisted of 32,955 nodes and 27,936 elements. Elements used were 8-node linear bricks with reduced integration (C3D8R). Each beam has a length of 609.6 millimeters and a cross-section of 38.1-mm by 38.1-mm. A zero vertical displacement boundary condition was placed at 50.8 millimeters inwards from both ends, resulting in a span length of 508 millimeters, simulating the physical experiments. Material properties were defined with the 4.5% MC properties reflecting the MC of the bending specimens. Material density was defined as $1,001 \text{ kg/m}^3$. A pressure load was applied at midspan of 110 Mpa over an area of 31.75-mm by 2.54-mm to have a resulting load of 8.90 kN. The compression test results for the 4.5% MC specimens were used to define the elastic moduli, shear moduli, and Poisson's ratios. The elastic moduli were defined

for E_L , E_R , and E_T as 30.4 GPa, 1.59 GPa, and 1.95 GPa, respectively. The shear moduli were defined for G_{LR} , G_{LT} , and G_{RT} as 0.98 GPa, 1.34 GPa, and 6.82 GPa, respectively. The Poisson's ratios were defined for ν_{LR} , ν_{LT} , and ν_{RT} , as 0.550, 0.587, and 0.477, respectively. The longitudinal direction was defined to be along the length of the beam.

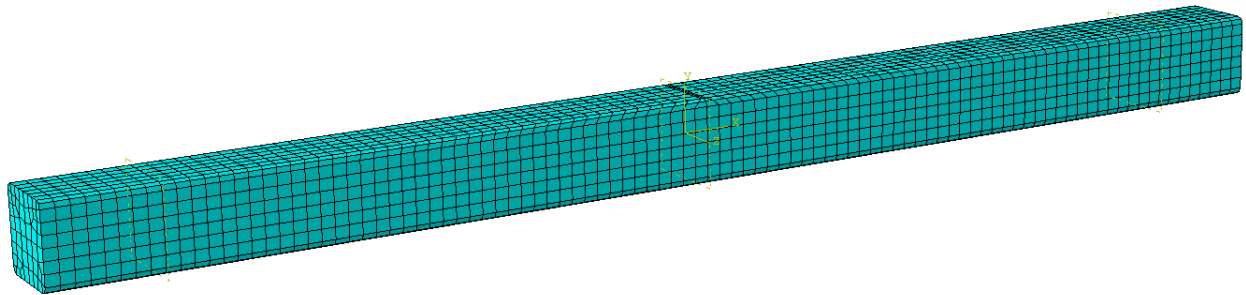


Figure 23: Coarse Mesh of Beam Validation Model

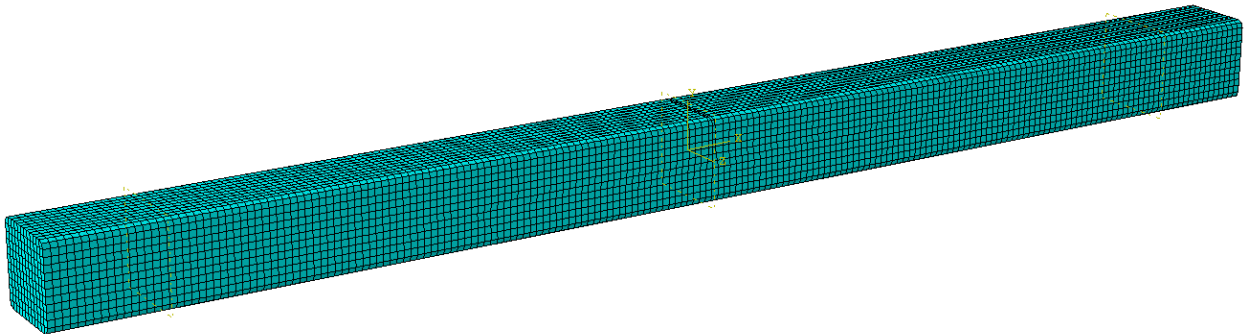


Figure 24: Fine Mesh of Beam Validation Model

Initial deflections obtained from the coarse and fine models were 5.72 mm and 5.66 mm, respectively, which did not agree with the experimental deflection of 7.72 mm. The model result was too stiff compared to the experimental tests. Two more models were then analyzed with changes to assess the sensitivity of the midspan deflection to the longitudinal modulus. The second model ran with the modulus set at the calculated bending modulus of 17.9 GPa, and the third model was ran iteratively to match the experimental deflection of 7.72 mm. Results of these models are tabulated in Table 9. Based on these models, the longitudinal modulus should

be 22.0 GPa to match the results obtained from the 3-point bending tests. To compare, the compression tests gave a longitudinal modulus of 30.5 GPa. That is a 29% difference.

Table 10: Initial Validation Modelling Results, with Varying Moduli Inputs

	E_L (GPa)	Deflection (mm)		E_L (GPa)	Deflection (mm)
Coarse Mesh	17.9	9.02	Fine Mesh	17.9	8.89
	22.0	7.49		21.7	7.42
	30.5	5.72		30.5	5.66

Upon observation of the Ipe samples, the direction of the fibers in relation to the direction of the span varied. Preliminary measurements determined that they vary up to 14 degrees off of the span’s direction with an average of approximately 6 degrees. Adjustments were then made to the direction of the axes within the validation model to reflect the “imperfect” orientation of the fiber directions. This was done by adjusting the material property directions (via local coordinates within the Abaqus CAE environment). With the longitudinal axes at 6 degrees off the length of the beam in both the radial and tangential directions, the finite element analysis provided more agreeable results (Table 10).

Table 11: Validation Modelling Results, with Adjusted Local Material Axes

	E_L (GPa)	Deflection (mm)		E_L (GPa)	Deflection (mm)
Coarse Model	30.5	7.26	Fine Model	30.5	7.13

3.3 MODELLING OF PROTOTYPE BARRIERS

To determine possible roadside barrier configurations using Ipe, finite element analysis was performed on various models. All geometry/mesh generations and post-processing was done via

the Abaqus CAE (v6.13) environment. Analysis was performed using the Abaqus/Explicit component of the Suite. An initial model was created with the commonly used steel W-beam barrier configuration. Multiple models were then created with various Ipe-based configurations, with various vehicular mass and velocities.

From the results of the analysis, the vehicle's lateral displacements, vehicle's velocities, vehicle's accelerations, and stress data and locations of interest were extracted over 0.01 second increments over the length of the impact. In the guardrail assessment literature, it is commonplace to analysis the vehicle data's displacement, velocity, and acceleration to determine the effectiveness of the barrier. Also, stress data for the barriers will be used to asses when and where failure occurs. Details of the modelling geometry, analysis, and post-processing are covered in the following sections.

3.3.1 Geometry and Meshing

The geometry of the barrier model is comprised of 5 main parts: the rail, posts, offset blocks, soil, vehicle, and road. Rail modelling was dependent on the type of railing. Steel W-beam railings were modelled with reduced integration, quadrilateral shell elements (S4R) with a 4mm thickness, based on the design drawings given in the AASHTO Roadside Design Guide. Each steel W-beam rail span consisted of 294 nodes and 260 elements. The cross-section geometry of the W-beam can be seen in Figure 25. The material properties for the steel W-beam were defined based on the A588 steel (weathering steel) properties with a density of 7860 kg/m^3 (490 lb/ft^3), Young's Modulus of 210GPa ($30,000 \text{ ksi}$), Poisson's Ratio of 0.3, yield strength of 485 MPa (50 ksi) and piecewise plasticity definitions that best fit the A588 stress-strain curve.

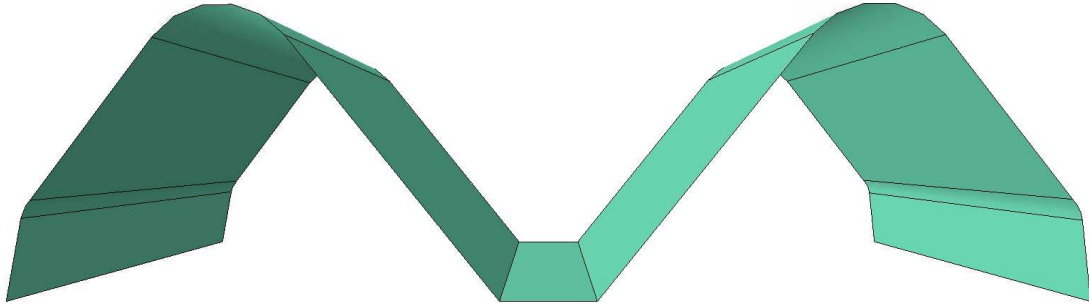


Figure 25: Cross-section of Steel W-beam

Ipe components were modelled with reduced integrated, 8-noded linear elements (C3D8R). Number of nodes and elements per rail span length is dependent on the configuration type and is covered later. Material physical and elastic properties obtained from the 4.5% MC material testing were used for the material definition. Abaqus does allow for a comprehensive analysis of failure in materials. For orthotropic materials, Tsai-Wu failure criterion is commonly used to develop the failure envelop. Abaqus does provide failure data based on the Tsai-Wu criterion, though this requires the yield strengths in all three primary directions. Testing performed on Ipe was limited based on availability of supplies and thus, these strengths were not determined. Failure will be assessed based on the destructive three-point bending tests performed earlier where the maximum bending stresses can be determined.

Geometry of the CFRP was done in 2-meter length, 0.09-meter wide strips. Each strip consisted of 4,020 nodes and 4,000 elements. CFRP strips were modelled with reduced integrated quadrilateral shell elements (S4R). To attach the shell elements to the 3D Ipe elements, a shell-to-solid coupling constraint is defined in Abaqus CAE. As described by the Abaqus documentation, shell-to-solid coupling “uses a set of internally defined distributing coupling constraints to couple the motion of ‘line’ of nodes along the edge of a shell model to the motion

of a set of nodes on a solid surface.” Material properties were obtained from Fyfe’s material data sheet. CFRP density was defined as 1740 kg/m^3 (109 lb/ft^3). Material properties were defined as a lamina, with E_1 at 82 GPa (11,900 ksi), E_2 at 10 GPa (1,450 ksi), ν_{12} at 0.30, and G_{12} at 5 GPa (725 ksi). Each

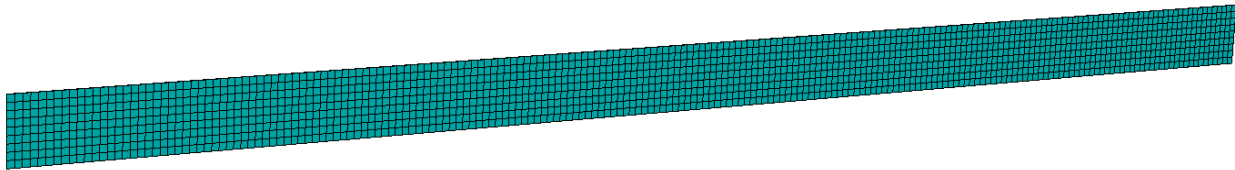


Figure 26: CFRP Strip (90mm) Geometry

Posts and offset blocks were modelled as Southern Pine; a commonly used type of wood in many barrier configurations (AASHTO 2010). Orthotropic material properties for Southern Pine were taken from the Wood Handbook (FPL 2010). Posts are embedded into the soil, while the offset blocks connect the posts to the railing as seen in Figure 24. Each post consisted of 189 nodes and 80 elements while the offset blocks consisted of 64 nodes and 27 elements. Reduced integrated 8-noded element blocks were used to model the posts and offset blocks (C3D8R).

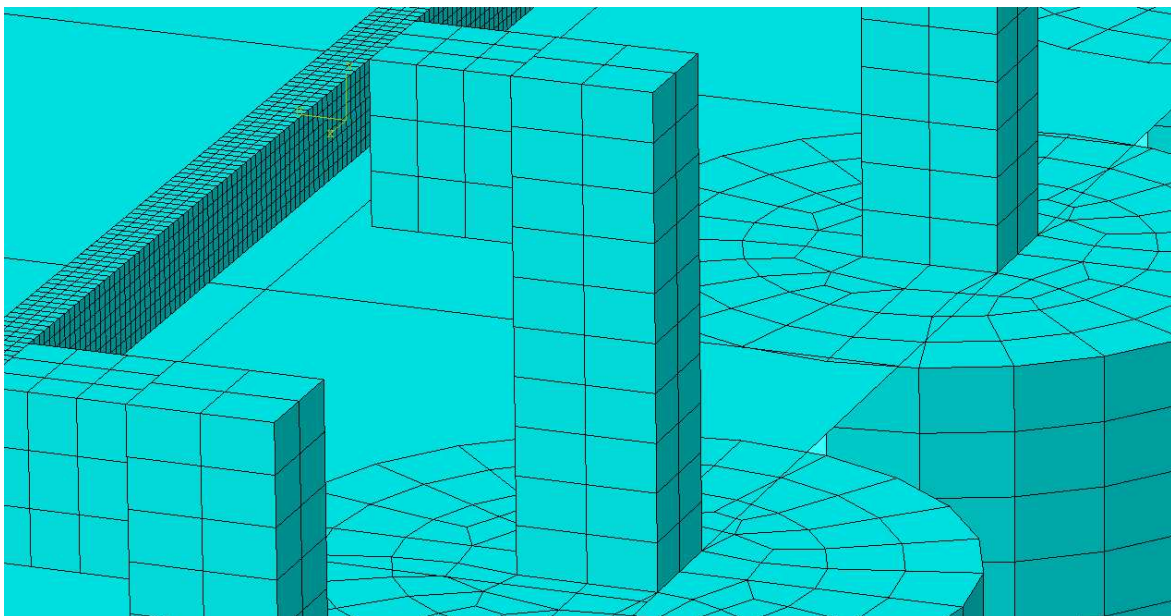


Figure 27: Post and Offset Block Geometry

Soil was modelled as 2-meter-long cylindrical blocks with a diameter of 1 meter, similar to the models ran by Whitworth et al. (2004). A hole is placed within the center to allow the post to be embedded 1 meter down its center. Geometry is shown in Figure 25 with each instance of the soil part containing 1,598 nodes and 1,288 elements. Reduced integrated 8-noded element blocks (C3D8R) were used. Isotropic properties were inputted to reflect loose to medium density “sandy” soils. Inputted density was 2100 kg/m^3 (101 lb/ft^3). Inputted elastic modulus was 20MPa with a Poisson Ratio of 0.3.

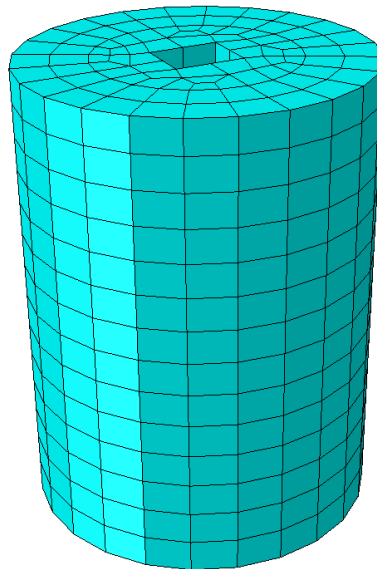


Figure 28: Soil Geometry

The vehicle was modelled as a whole block similar to the model created by Shen et al. (2008). Geometry is shown in Figure 29 with 1,869 nodes and 1,416 elements. The overall size of the vehicle was 4.8 meters x 1.7 meters x 1.5 meters. Densities were defined as 125 kg/m^3 for a 1,500 kg vehicle or 73.1 kg/m^3 for a 895 kg vehicle. The vehicle was modelled as an isotropic aluminum material, with an elastic modulus of 69 GPa and a Poisson’s Ratio of 0.32.

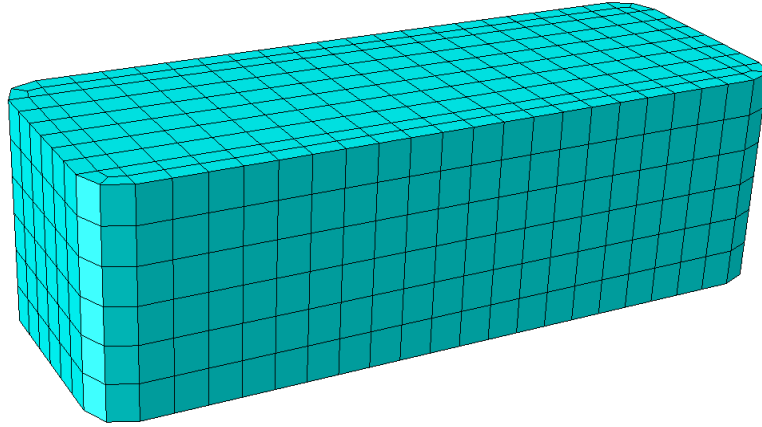


Figure 29: Vehicle Geometry

The road was modelled as one rigid shell plane. As a rigid part, neither elements nor material properties were needed nor defined for the road. All parts were then assembled within Abaqus CAE to set up the overall geometry of the model similar to the models created by Shen et al. (2008) and Whitworth et al. (2004). The overall model consisted of 9 posts, allowing for 8 2-meter barrier spans (Figures 27 and 28).

In this model, there are two CIPs as noted by NCHRP: “one that produces the greatest potential for vehicular pocketing or wheel snagging and one that produces the greatest loading on a critical part of the barrier, such as at a rail splice” (NCHRP 1993). Since vehicular pocketing and wheel snagging analysis is outside of the scope of this research, the splicing locations at the rail posts were the CIPs for the model. Thus, the vehicle is oriented with its centerline intersecting the splice location. As per NCHRP Report 350, the vehicle is oriented 20 degrees off of the guardrail.

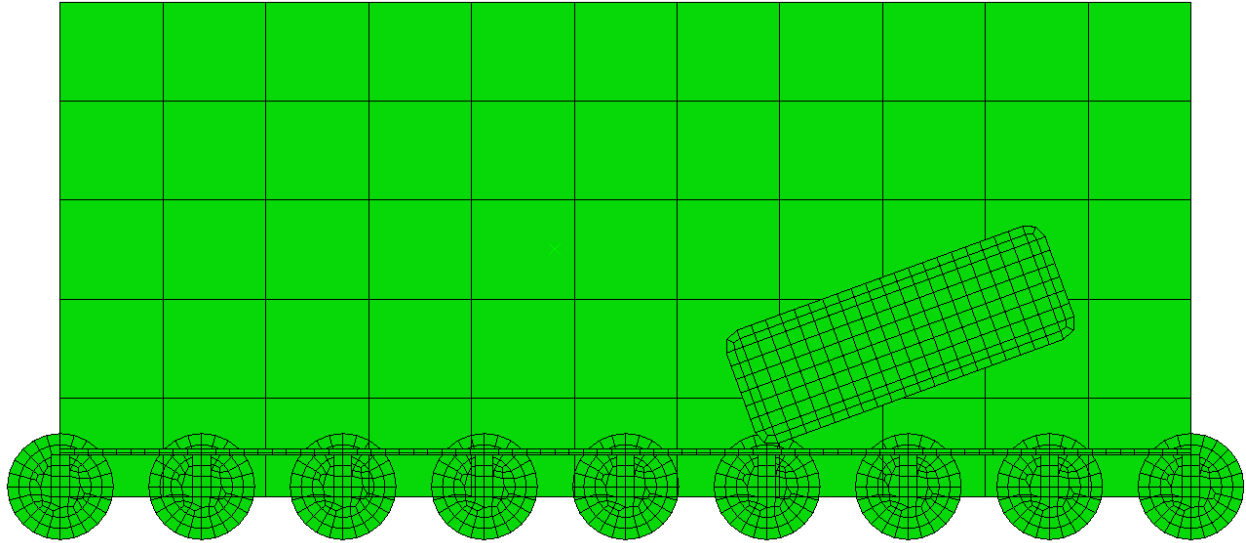


Figure 30: Top-down (Plan) View of Overall Model with Steel W-Beam Railing

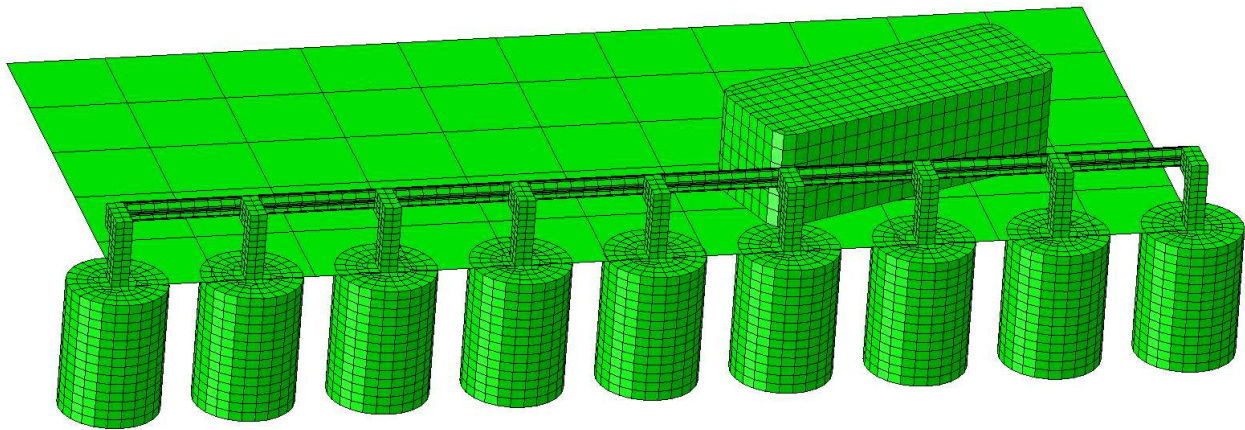


Figure 31: General View of Overall Model with Steel W-Beam Railing

3.3.2 Analysis Set-up

Setting up the analysis in Abaqus involved defining the time-steps, model constraints, interactions between objects, and various boundary conditions. It is crucial to ensure proper definitions are used to obtain usable results and to reflect real-world behavior. A total of four impact scenarios are used for each configuration and are highlighted in Table 11. Scenario 1 was created to parallel the work done by Shen et al, where the testing criteria was presumably based

on EN-1317 with their use of the 1,500 kg vehicle mass, but with a slightly higher impact speed of 100 km/hr. Scenarios 2 through 4 utilizes a lighter vehicle of 895 kg with impact speeds of 100 km/hr, 70 km/hr, and 50 km/hr. This combination of mass and speeds are some of the impact conditions outlined by NCHRP for their standardized testing criteria. Each impact scenario is ran over a period of 0.2 seconds, with 0.01-second time steps.

Table 12: Impact Scenarios

Scenario Number	Vehicular Mass	Vehicular Impact Speed
1	1,500 kg	100 km/hr
2	895 kg	100 km/hr
3	895 kg	70 km/hr
4	895 kg	50 km/hr

3.3.3 Constraints, Loading, and Boundary Conditions

For proper analysis of the meshes generated from the geometry, constraints, loading, and boundary conditions must be defined. All constraints, contact behavior, and other interactions are done within the interaction module of Abaqus CAE. All loadings, fields, and boundary conditions were done within the load module.

Constraints were utilized with the “tie” function in Abaqus CAE. Ties are used to define surfaces in which there is no desirable relative motion between them. In reality, connections such as bolts will be used to piece the parts together. The analysis of those types of connections is outside the scope of this research, thus tie constraints were utilized. Ties were defined between the posts and offset blocks, the offset blocks and the railing, and CFRP layers to both offset blocks and railings where applicable. Following the constraints, three interactions were

defined. Firstly, a surface-to-surface contact between the vehicle and the rigid road was defined with a friction coefficient of 0.7. Secondly, a surface-to-surface contact between the posts and soil was also defined with the same friction coefficient of 0.7. It was later found that this contact between the posts and soil had negligible effect on the overall impact. Thirdly, a general contact was defined for all other parts within the assembly with the friction coefficient of 0.2. This was to ensure that all surfaces of elements within the model will not intersect, i.e. two physical objects can't exist in the same space.

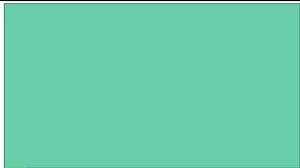
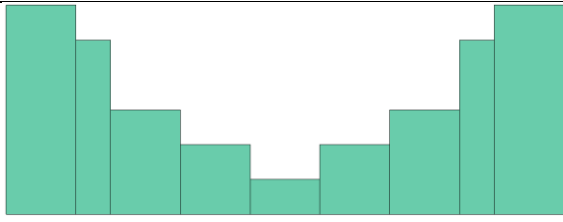
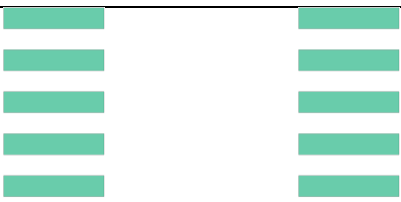
Two definitions were made within the loading module. Firstly, a gravitational force was applied to the vehicle of 9.81 m/s^2 . Secondly, a velocity field was applied to the vehicle at speeds of 100km/hr, 70 km/hr, and 50 km/hr. A boundary condition was placed at the far ends of the railings to have zero displacements about all axes. It was assumed that railings far away (4 posts or 8 meters from either end) from the impact point are assumed to have negligible displacements. Another boundary condition was placed on the edges of the cylindrical soil parts, with zero displacements and zero rotations about all axes.

3.3.4 Railing Configurations

A total of 8 different rail configurations were modelled. Included in this was the commonly used steel W-beam rail to be used as a comparison. Rail configurations are listed in Table 13 with their labels, descriptions, cross-sections and price per linear meter. Pricing for Ipe was determined based on the price for a standard Ipe board of \$7.51/m at a local distributor. Pricing for CFRP was determined based on average online distributor sites at \$10.04/m for a 90mm wide strip.

Development of the rail configurations was done iteratively and started with a bulkier cross-section, labelled Ipe-A, similar to the development by Davids et al. (2006). Ipe-A-CFRP utilized the same geometry as the Ipe-A with an added layer of CFRP. Ipe-B, Ipe-C, and Ipe-CFRP were developed to determine performance based on a lower cost, i.e. a smaller cross-section. Ipe-B and Ipe-C were simple configurations with a cross-section consisting of 2 and 4 boards, respectively. Ipe-C-CFRP added 4-90mm CFRP strips to the cross-section. Ipe-D was created using the same amount of material from Ipe-A, but with a modified geometry. The new geometry for Ipe D is based off of the study by Banks et al. (2001), where the “pocketed” shape of the railing provided desirable results. Ipe-E was developed with the idea of progressive resistance, where the area of the cross-section would increase due to consecutive layers becoming “active” over a length of time, thus increasing the rail’s moment of inertia and subsequently, its resistance.

Table 13: Model Rail Configurations

Rail	Description	Cross-Section View	Price/meter (\$)
Steel W-beam	Specs based on AASHTO Roadside Design Guide		15.62
“Ipe-A”	100x180(mm) One bulky layup of Ipe		75.33
“Ipe-A-CFRP”	100x180(mm) Ipe-A layup with CFRP		95.44
“Ipe-B”	2 – 19x89mm (standard boards available from distributors)		15.03
“Ipe-C”	4 – 19x89mm (double the amount of Ipe-B)		30.05
“Ipe-C-CFRP”	Ipe-C layup with CFRP attached		70.24
“Ipe-D”	Same cross-sectional area as Ipe-A with config similar to Bank (2001)		75.33
“Ipe-E”	2 – 5 boards with 19mm spacing.		76.38

3.3.5 Model Results and Discussion

For each impact scenario, kinematic and stress data were extracted. Plots were then constructed from that data to compare performance between the various railing configurations. Displacement versus time plots and plan view snapshots are provided within Figure 32 through Figure 36 in the following pages. Additional time-lapse figures of each impact scenario are shown in Appendix A.

Ipe-B, Ipe-C, and Ipe-C-CFRP railing configurations had a lack of usable results. All three lacked the amount of material and/or resistance to redirect the vehicle. This resulted in the posts, and subsequently the soil, to resist and absorb the impact. Thus, these configurations were discarded from consideration.

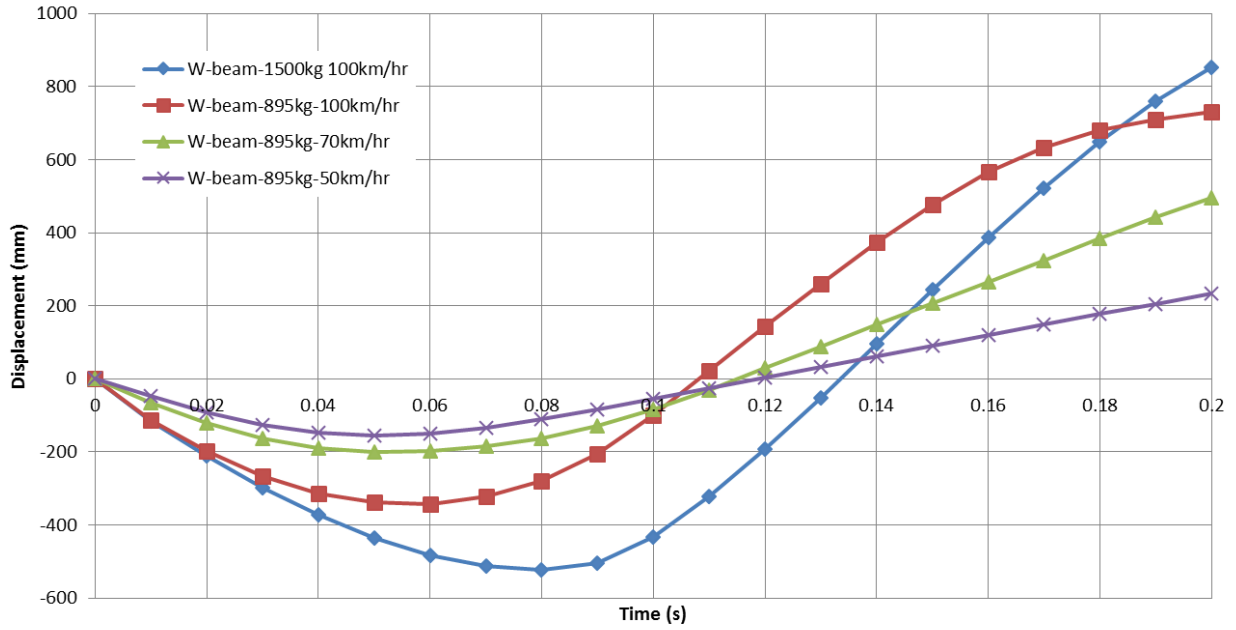


Figure 32: Steel W-Beam – Displacement versus Time

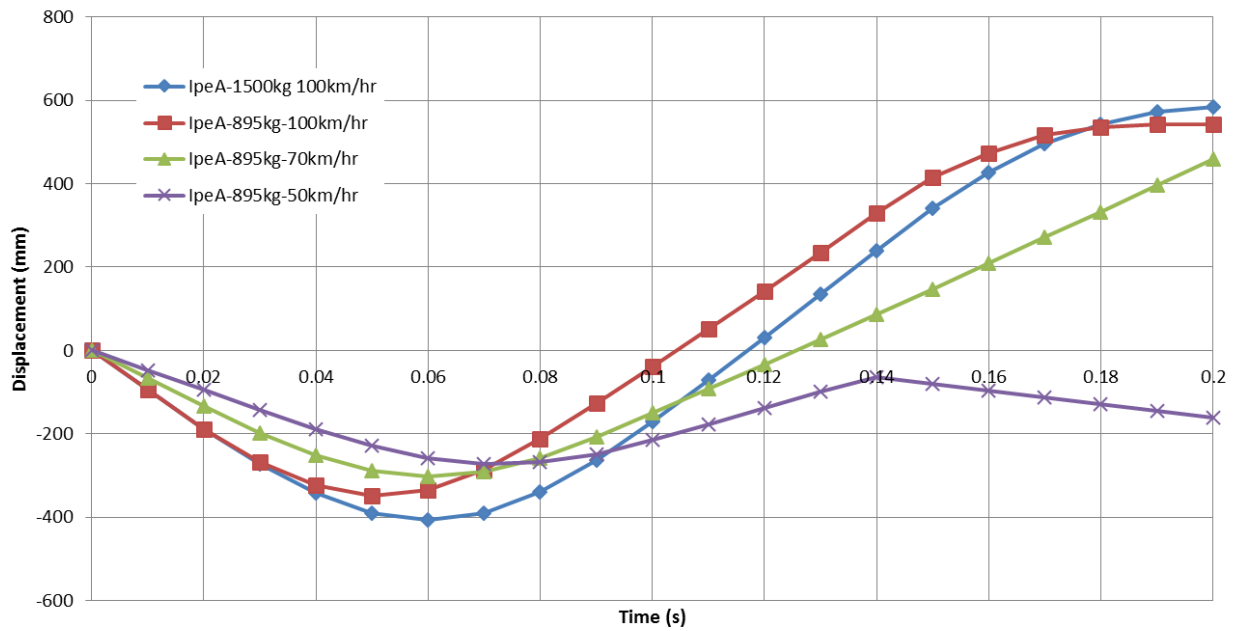


Figure 33: Ipe-A – Displacement versus Time

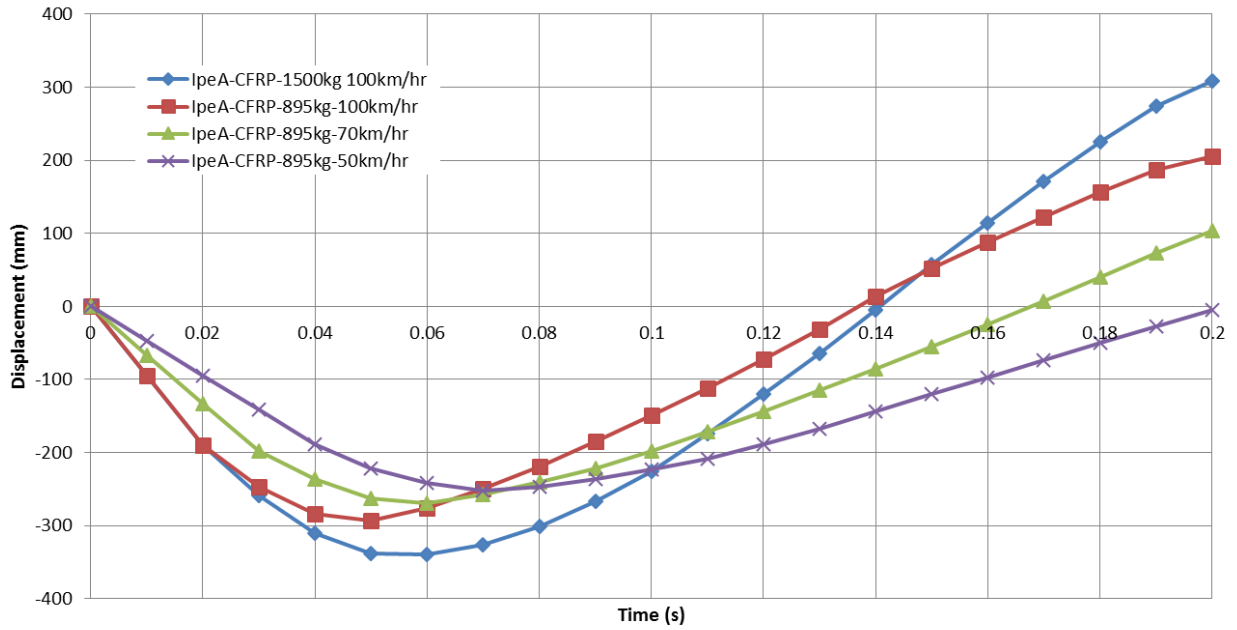


Figure 34: IpeA-CFRP – Displacement Versus Time

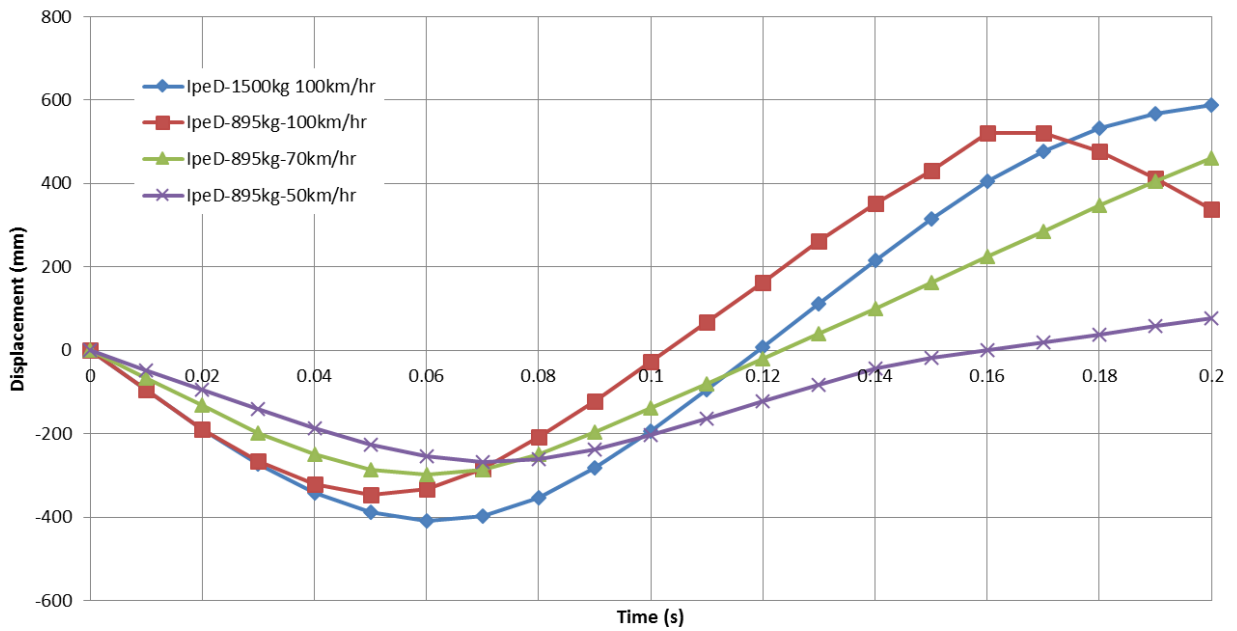


Figure 35: IpeD – Displacement Versus Time

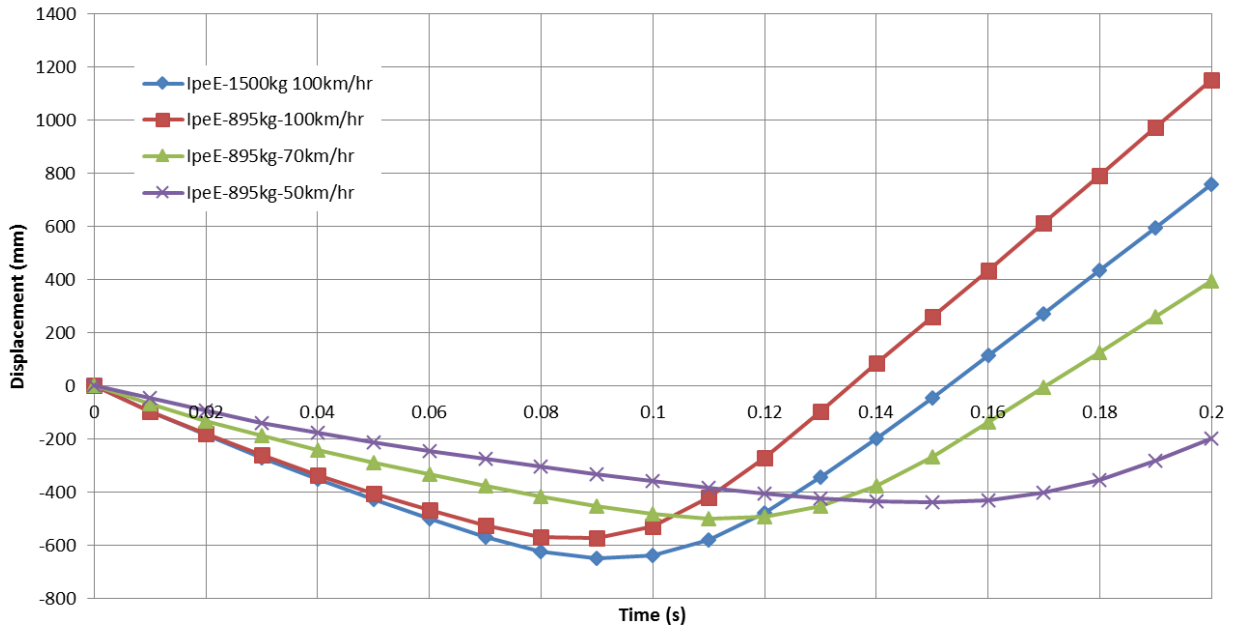


Figure 36: Ipe-E – Displacement Versus Time

Finite element modelling of the steel W-beam shows a maximum lateral deflection of 0.523 meters with a 1,500 kg vehicle. From experimental results as mentioned in the Roadside Design Guide, a 2,000 kg vehicle would result in having a maximum lateral deflection of 0.8 meters (AASHTO 2002). A 0.523-meter deflection from the model is reasonable and will be used as a comparison for the all impact scenarios.

Ipe-A was the first model. Due to its bulky cross-section, it was expected to be relatively stiff. Maximum deflections were 406 mm, 347 mm, 303 mm, and 272 mm for impact scenarios 1, 2, 3, and 4, respectively. Maximum stresses within the Ipe material were 209.56 MPa, 147.36 MPa, 82.34 MPa, and 55.48 MPa. Ipe-A failed solely in impact scenario 1. For impact scenario 4, the vehicle tilted toward one side, causing heavy friction against the side closest to the railing. This resulted in a sudden change of momentum as seen in the plots above. Compared to the steel

W-beam, Ipe-A is relatively stiff. With an addition of a CFRP layer, Ipe-A-CFRP's maximum deflections were 340 mm, 293 mm, 269 mm, and 253 mm for impact scenarios 1, 2, 3, and 4, respectively. Maximum stresses within the Ipe material were 174.98 MPa, 135.16 MPa, 85.60 MPa, and 78.19 MPa, respectively. Maximum stresses within the CFRP material were 751.59 MPa, 500.16 MPa, 358.84 MPa, and 228.83 MPa, respectively. Adding the CFRP layer resulted in lower lateral displacements and lower stress within the Ipe material.

Ipe-D utilized the findings by Bank et al. (2001) to assess if the same principles applied to an Ipe cross-section would have desirable results. Maximum deflections for Ipe-D were 410 mm, 346 mm, 299 mm, and 267 mm for impact scenarios 1, 2, 3, and 4, respectively. Maximum stresses within the Ipe material were 248.93 MPa, 172.08 MPa, 76.21 MPa, and 47.45 MPa, respectively. Ipe-D failed solely in impact scenario 1. Because of the geometry of the cross-section, immediate crushing of the railing occurred at the moment of impact for all four scenarios. Compared to the flexibility of the steel W-beam, Ipe-D was stiffer for scenario 1, and more flexible in scenarios 3 and 4. Scenario two resulted in the same lateral deflections.

Ipe-E's maximum deflections were 650 mm, 574 mm, 498 mm, and 439 mm for impact scenarios 1, 2, 3, and 4, respectively. Maximum stresses within the Ipe material were 296.62 MPa, 249.06 MPa, 164.41 MPa, and 134.98 MPa, respectively. Ipe-E failed in impact scenarios 1 and 2 due to stresses at the connection between the Ipe railing and the offset blocks. Compared to the other models, Ipe-E had the most dynamic results due to the multiple layers. During the impact scenarios, it was observed that the main rail to absorb the energy of the vehicle performed as intended. It was also observed that the railings immediately adjacent to the main rail had a

significant amount of movement. This behavior in the rail gets diminished the further away from the impact point the rails are. Also, Ipe-E tends to “fling” the vehicle back toward the road rather than permanently absorbing the impact energy. Safety is a concern for Ipe-E’s configuration. Compared to the flexibility of the steel W-beam, Ipe-E was more flexible in all four scenarios.

A summary of the maximum displacements and maximum stresses are shown in Tables 14 and 15. Displacements are shown along with the steel W-beam as a comparison. Stresses are highlighted in red in Table 15 when they are above the failure bending stress of 208 MPa for Ipe or the failure tensile stress of 986 MPa for CFRP. Failure criteria for Ipe was based on the experimental three-point bending test. Failure criteria for CFRP was based on the company’s published material data sheet.

Table 14: Maximum Displacement Results

Max Disp (mm)	Scenario 1	Scenario 2	Scenario 3	Scenario 4
Ipe-A	266	208	303	272
Ipe-A-CFRP	340	293	269	253
Ipe-D	410	346	299	267
Ipe-E	650	574	498	439
Steel W-beam	523	343	201	156

Table 15: Maximum Stress Results

Max Stresses (Mpa)	Scenario 1	Scenario 2	Scenario 3	Scenario 4
Ipe-A	209.56	147.36	82.34	55.48
Ipe-A-CFRP (Ipe)	174.98	135.16	85.60	78.19
Ipe-A-CFRP (CFRP)	751.59	500.16	358.84	228.83
Ipe-D	248.93	172.08	76.21	47.45
Ipe-E	296.62	249.06	164.41	134.98
Steel W-beam	392.89	392.26	400.88	331.84

Additional plots were created to assess the relative differences in the performance between the railing configurations. These plots are separated by the associated impact scenario. Figures 53, 54, 55, and 56 are plots of displacement versus time for impact scenarios 1, 2, 3, and 4. Each plot contains five different configurations: Ipe-A, Ipe-A-CFRP, Ipe-D, Ipe-E, and the steel W-beam.

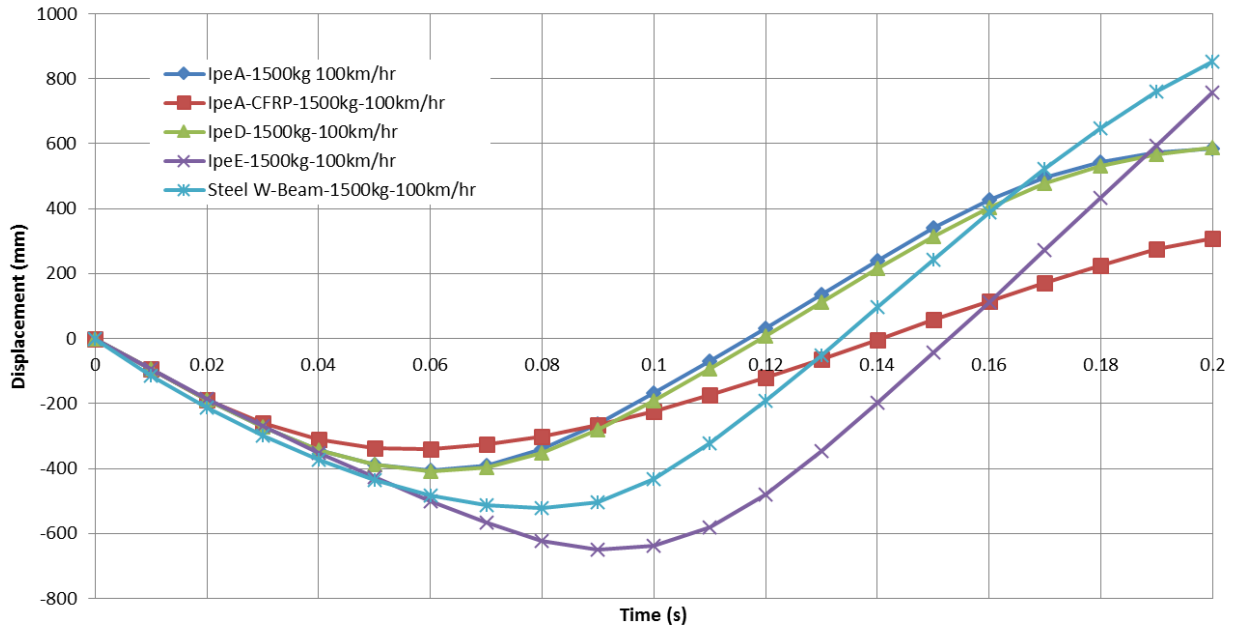


Figure 37: Performance Comparison – 1,500 kg @ 100km/hr

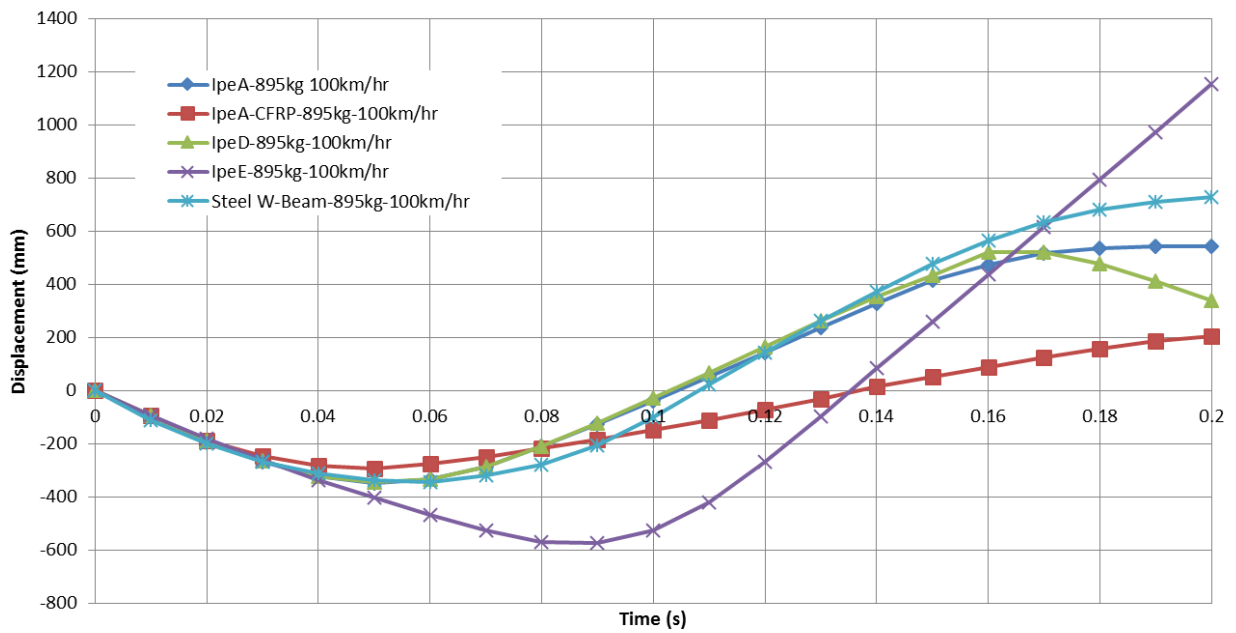


Figure 38: Performance Comparison – 895 kg @ 100km/hr

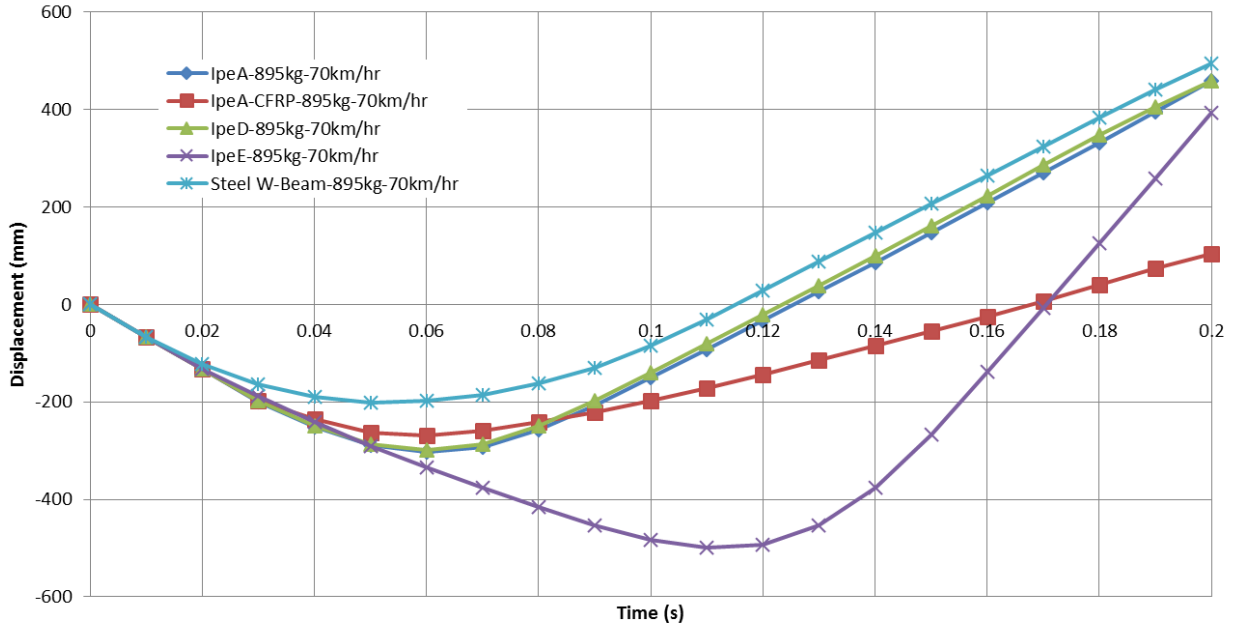


Figure 39: Performance Comparison – 895 kg @ 70km/hr

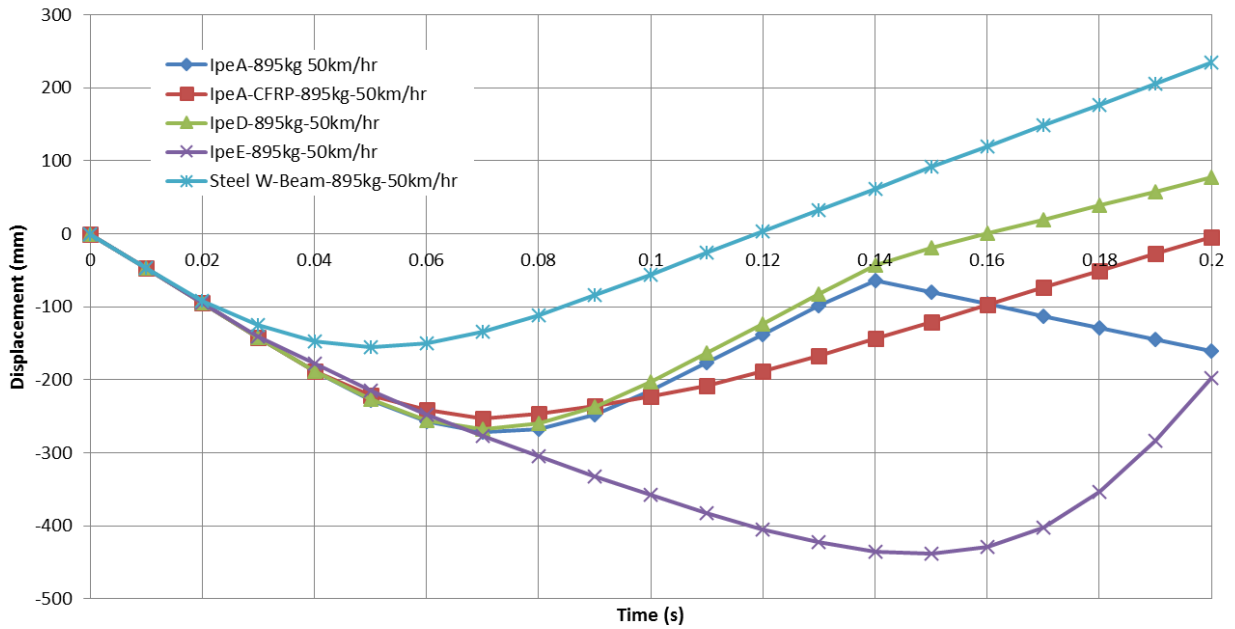


Figure 40: Performance Comparison – 895 kg @ 50km/hr

For impact scenario 1 (1,500 kg vehicle with impact speed of 100km/hr), Ipe-A, Ipe-A-CFRP, and Ipe-D were all stiffer than the steel W-beam, with Ipe-A-CFRP being the stiffest. Ipe-A and

Ipe-D, both of which have the same amount of material within their cross-section, performed similarly. Ipe-E was very flexible by allowing a lateral deflection of 650 mm where the steel W-beam had a lateral deflection of 523 mm (24% difference). To reiterate, Ipe-A, Ipe-D, and Ipe-E all had stresses beyond their strength, implying that replacement rails would be needed with a crash of this magnitude and scale. Consequently, the lifetime costs for these railing configurations would be higher.

For impact scenario 2 (895 kg vehicle with impact speed of 100km/hr), Ipe-A, Ipe-A-CFRP, and Ipe-D were all stiffer than the steel W-beam, with Ipe-A-CFRP being the stiffest. Ipe-A and Ipe-D performed very similarly to the steel W-beam in terms of maximum deflection. While Ipe-A-CFRP was the stiffest, it also deflected the vehicle towards the road the least as seen in Figure 54. This behavior could be a result of a very idealized model of the vehicle itself, rather than the complex geometry of actual vehicular bodies. Ipe E was very flexible by allowing a lateral deflection of 574 mm where the steel W-beam had a lateral deflection of 343 mm (67% difference). Ipe-E was the only railing configuration that had stresses above its strength, implying higher lifetime costs than the others.

For impact scenario 3 (895 kg vehicle with impact speed of 70km/hr) and impact scenario 4 (895 kg vehicle with impact speed of 50km/hr), all Ipe-based rail configurations were less stiff than the steel W-beam. Ipe-A and Ipe-D once again performed similarly for both scenarios. Ipe E was very flexible in both scenarios 3 and 4 by allowing a lateral deflection of 498 mm and 439 mm where the steel W-beam had a lateral deflection of 201 mm (148% difference) and 156 mm (181% difference), respectively. For environments where the speed of traffic is lower, all railing

configurations were able to properly contain the vehicle and redirect it without any major failures.

Two railing configurations were modified to have a layer of CFRP on the backside to assess its performance: Ipe-A and Ipe-C. Ipe-C's results were not usable as mentioned earlier. For Ipe-A, the addition of CFRP reduced the deflections for impact scenarios 1, 2, 3, and 4 from 406 mm, 347 mm, 303 mm, and 272 mm to 340 mm, 293 mm, 269 mm, and 253 mm, respectively (Table 16). This results in decreases of 16.3%, 15.6%, 11.2%, and 7.0%. Adding the layer of CFRP to the backside of the Ipe-A railing had an estimated cost of 20 dollars per linear foot, an increase of 26.7% in costs. Unless use of space is very important, simply adding additional Ipe layers would provide more resistance at less of a cost.

Table 16: Comparison of Ipe-A and Ipe-A-CFRP

Impact Scenario	Ipe-A	Ipe-A-CFRP	Difference
1	406 mm	340 mm	-16.3%
2	347 mm	293 mm	-15.6%
3	303 mm	269 mm	-11.2%
4	272 mm	253 mm	-7.0%

There are an infinite number of variations of cross-sections that could be considered for this type of analysis, and the above were chosen to get the overall behavior of how Ipe would respond in various impact scenarios. Recommendations for more cross-sections are as follows:

- Modification of the Ipe-A rail to contain a weaker (and less expensive) material in the center. This would still concentrate the high bending stresses to the outer Ipe layers, while placing the lower bending stresses to the new materials.
- Modification of the Ipe-D rail to assess the material in the center. This could be done in the form of replacing the material as mentioned in the bullet above, or just simply removing it.
- Modification of the Ipe-E rail to change the distance between the boards. A smaller distance is recommended to attempt to reduce the dynamic motions of each rail board during the scenarios.

It is important to note that these models are fairly idealized when compared to the complexity of real world geometry. For longitudinal barriers such as the ones modelled for this paper, the CIP is located at the posts. At these points, connections can be the main point of failure rather than the railing. Also, the complex nature of vehicles and their numerous mechanical parts could cause some wheel snagging and other unpredictable events will need to be analyzed. Thus, before actual implementation of any of these railings, it is recommended that a full-scale test be performed using the criteria contained in NCHRP Report 350 or EN-1317 to understand the full behavior of all the dynamic parts.

Ipe can perform similarly to the commonly used steel W-beam railing. The main differences relate to their behavior at varying impact speeds and cost. The major drawback with Ipe barriers lie in the cost associated with them. Ipe railings that were modelled for this study would run approximately 5 times as much in cost than the steel W-beam rails to achieve similar

performance. Realistic implementation of Ipe barriers would be more beneficial for roads with lower speed limits. Less material would be required for the slower speeds, thus lowering the cost. Implementation of CFRP did not increase the performance of the railings to justify its cost.

CHAPTER 4 – CONCLUSION

This study was split into two main parts: determining the material properties of the wood material, Ipe, and to determine its viability in its use in roadside barriers. Various testing methods were used to determine the material properties: three-point bending, compressions, impact resonance, and resonance ultrasonic spectroscopy (RUS). Compression tests were done at 4.5% and 8.0% moisture contents. Three-point bending and compression tests were successful to extract the bending modulus, elastic moduli along the three principle directions, shear moduli, and Poisson ratios. From here, the entire stiffness matrix was able to be determined for Ipe at both moisture contents.

Finite element analysis of vehicular impact scenarios makes up the second part of this study. Multiple Ipe-based configurations were developed within Abaqus CAE and placed under four different impact scenarios. When compared to the commonly used steel W beam guardrail, Ipe's relative responses varied based on the impact scenario. Impacts that involved more energy (more mass and/or higher velocity) resulted in the Ipe railing configurations to be stiffer than the steel W-beam. The Ipe-A railing configuration deflected 266 mm while the steel W-beam deflected 523 mm for the scenario with the 1,500 kg vehicle impacting at 100 km/hr. Impacts that involved less energy (less mass and/or lower velocity) resulted in the Ipe railing configurations to become more flexible. The same Ipe-A railing deflected 272 mm while the steel W-beam deflected 156 mm for the scenario with the 895 kg vehicle impacting at 50 km/hr. The Ipe-A, Ipe-A-CFRP, Ipe-D, and Ipe-E configurations showed the same relative behavior

with the exception of the Ipe-E for the 1,500 kg vehicle at 100 km/hr scenario. From a deflection standpoint, Ipe can perform just as well as the commonly used steel W-beam.

When considering stresses for the 1,500 kg vehicle at 100 km/hr, the Ipe-A, Ipe-D and Ipe-E railings showed maximum stresses that exceeded Ipe's bending strength of 208 MPa. With the inclusion of the CFRP to the Ipe-A railing, the Ipe remained below its bending strength. For the 895 kg vehicle at 100 km/hr, the Ipe-E showed a maximum stress of 120% of Ipe's bending strength. In the other impact scenarios, the Ipe remained below their respective bending strengths. For the steel W-beam, the results showed that the steel material was at or below the steel's ultimate bending strength of approximately 400 MPa. To summarize, the steel stresses ranged from 83% to 100% of the steel's ultimate strength while the Ipe stresses ranged from 27% to 120% of the Ipe's ultimate strength. It is important to note that steel typically yields at approximately 250 MPa or 63% of its ultimate strength, thus yielding of the steel W-beam is very likely in all four scenarios. Based on the material tests discussed earlier, Ipe's stress curve is relatively linear up to its bending strength. This implies that the Ipe is less likely to show yield or damage in an impact scenario involving lower speeds whereas the steel is more likely to yield and sustain damage in any impact scenario. For lower speed zones, Ipe would potentially require little maintenance over the course of its life than the steel W-beam from repairs.

One major drawback for implementing Ipe for roadside barriers would be its cost. Railing configurations that were able to perform similarly to the steel W-beam resulted in costs that is roughly 5 times as much. Ipe-A, Ipe-D, and Ipe-E runs at approximately \$75.33, \$75.33, and \$76.38 per linear meter. The steel W-beam runs at approximately \$15.62 per linear meter. Also,

some local distributors have been seeing a rise in Ipe's cost. The samples obtained from the distributor increased from \$9.84 per meter to \$11.28 per meter over two years due to demand. This equates to a cost increase of approximately 15%. According to the distributor, this cost increase is reflective of the overall Ipe market due to high demand.

With the inclusion of CFRP to the Ipe-A configuration, maximum deflections increased for the scenarios involving vehicles with speeds of 100 km/hr by 28% for the 1,500 kg vehicle and 41% for the 895 kg vehicle. Decreases in maximum deflections resulted for the lower speeds by 11% for the 70 km/hr scenario and 7% for the 50 km/hr scenario, both involving an 895 kg vehicle. Stresses within the Ipe for the 100 km/hr scenarios decreased by 23% for the 1,500 kg vehicle and 8% for the 895 kg vehicle. Stresses within the Ipe for the 70 km/hr and 50 km/hr scenarios increased by 4% and 41%, respectively. Cost-wise, the inclusion of CFRP to the Ipe-A configuration would cost an additional \$20.11 per linear meter: an increase of 27%. While the inclusion of CFRP did decrease the stresses within the Ipe material for the 100 km/hr scenarios, the percentage increase of 27% in price does not justify the variances in deflections and stresses for the other scenarios.

Ipe's potential to withstand yielding or damage during lower speed impact scenarios along with its natural environmental resistance could help alleviate that cost by reducing the frequency of repairs. Because of this, Ipe's use in roadside barriers would be more beneficial for rural areas where speeds are 50 km/hr or 70 km/hr, rather than the highway speeds of 100 km/hr. A smaller cross-section could be viable to save costs in these areas depending on the desirability of the barrier's flexibility. Even with the cross-sections used in this study, the Ipe barriers showed

more flexibility by deflecting more than the steel W-beams for those slower speeds. A higher deflection implies more room for the impact forces to transfer, thus potentially reducing the jerk and damage to the impacting vehicle. Also, rural areas with slower speeds would be more attractive for Ipe's implementation due to its well-known aesthetic appeal and natural environmental resistance.

To summarize, the major findings from this study are:

- Ipe can perform just as well as W-beam rails.
- To obtain a similar performance to W-beam rails, the cost for Ipe would run approximately 5 times as much for the configurations used in this study.
- Realistic implementation of Ipe barriers would be more beneficial for roads with lower speed limits, resulting in less required material and thus, lowering the cost.
- Lower speeds showed more flexibility, which could result in less damage to the impacting vehicle.
- Implementation of CFRP did not increase the performance of the railings to justify its cost.

For further research on this, a few recommendations and considerations are as follows:

- Create more samples to validate material properties via impact resonance and/or RUS
- Create more samples to get ultimate strengths in the radial and tangential directions. This would provide the variables needed to provide analysis with the Tsai-Wu failure criteria
- Develop full-scale tests to assess real-world behavior.

REFERENCES

1. American Association of State Highway and Transportation Officials (AASHTO). 2009. *Manual for Assessing Safety Hardware, 2009.*
2. American Association of State Highway and Transportation Officials (AASHTO). 2006. "Roadside Design Guide, 3rd Edition."
3. ABAQUS. 2011. ABAQUS Documentation', Dassault Systèmes, Providence, RI.
4. Ad, J M. 1999. "Literature Review of Impact Strength of Timber and Joints," 2–7.
5. Aira, José R., Francisco Arriaga, and Guillermo Íñiguez-González. 2014. "Determination of the Elastic Constants of Scots Pine (*Pinus Sylvestris* L.) Wood by Means of Compression Tests." *Biosystems Engineering* 126: 12–22.
6. ASTM Standard C33. 2003. "Specification for Concrete Aggregates," ASTM International, West Conshohocken, PA.
7. ASTM Standard D143. 2010 "Standard Test Methods for Small Clear Specimens of Timber." ASTM International, West Conshohocken, PA.
8. ASTM Standard E1876. 2009. "Standard Test Method for Dynamic Young's Modulus, Shear Modulus, and Poisson's Ratio by Impulse Excitation of Vibration," ASTM International, West Conshohocken, PA, 2003
9. Bank, L. C., and T. R. Gentry. 2001. "Development of a Pultruded Composite Material Highway Guardrail." *Composites - Part A: Applied Science and Manufacturing* 32: 1329–38.
10. Biehler, Allen D, Larry L Brown, William a V Clark, and David S Ekern. 2008. *Cooperative Highway Program. Traffic Safety. Vol. 22.*

11. Bodig, J., Jayne, B. A. 1993. *Mechanics of wood and wood composites*. Reprint ed. Malabar, Fla.: Krieger Pub.
12. Borri, Antonio, Marco Corradi, and Andrea Grazini. 2005. "A Method for Flexural Reinforcement of Old Wood Beams with CFRP Materials." *Composites Part B: Engineering* 36: 143–53.
13. Brajovic. 2006. "The Potential of Ipe" *Office* 31 (2): 185–214.
14. Consolazio, Gary R, and Jae H Chung. 1998. "Vehicle Impact Simulation for Curb and Barrier Design." *Simulation* I (October).
15. Davids, William G., Joshua K. Botting, and Michael Peterson. 2006. "Development and Structural Testing of a Composite-Reinforced Timber Highway Guardrail." *Construction and Building Materials* 20: 733–43.
16. Détienne, Pierre. 2011. "Les Espèces Du Genre *Tabebuia* Susceptibles de Fournir Le Bois D ' Ipé" 307 (1): 69–77.
17. Dutta, P. K. 2003. "An Investigation into the Design and Manufacture of FRP Composite W-Beam Guardrail."
18. Falk, Robert H., Derek G Maul, and Steven M Cramer. 2008. "Engineering Properties of Douglas-Fir Lumber Reclaimed from Deconstructed Buildings."
19. Forest Products Laboratory (FRL). 2010. *Wood Handbook: Wood as an Engineering Material. Agriculture*. Vol. 72.
20. Gand, Alfred Kofi, Tak Ming Chan, and James Toby Mottram. 2013. "Civil and Structural Engineering Applications, Recent Trends, Research and Developments on Pultruded Fiber Reinforced Polymer Closed Sections: A Review." *Frontiers of Structural and Civil Engineering* 7 (3): 227–44.

21. Jasieńko, Jerzy, and Tomasz P. Nowak. 2014. "Solid Timber Beams Strengthened with Steel Plates – Experimental Studies." *Construction and Building Materials* 63: 81–88.
22. Kerboua, B., E. Adda Bedia, and Tounsi, A. 2010. "Impact of the Fiber-Reinforced Plastic (FRP) and the Thermal Effect for the Interfacial Stresses." *Journal of Reinforced Plastics and Composites* 29 (6): 921–35.
23. Kok, A. 1997. "Lumped Impulses, Discrete Displacements and a Moving Load Analysis." *Heron* 42: 3–23.
24. Kretschmann, David E. 2010. "Chapter 5 - Mechanical Properties of Wood." In *Wood Handbook - Wood as an Engineering Material*, 1–46.
25. Leijten, A J M. 2004 "Heat Treated Wood and the Influence on the Impact Bending Strength" 49 (4): 349–59.
26. Lim, Jinah, Hyanmyeong Yeo, and Jun-jae Lee. 2012. "Impact Performance of Wood Guardrail for Bicycle Road." In *World Conference on Timber Engineering*.
27. Longo, R., T. Delaunay, D. Laux, M. El Mouridi, O. Arnould, and E. Le Clézio. 2012. "Wood Elastic Characterization from a Single Sample by Resonant Ultrasound Spectroscopy." *Ultrasonics* 52 (8). Elsevier B.V.: 971–74.
28. Lorenzis, Laura. 2012. "Some Recent Results and Open Issues on Interface Modeling in Civil Engineering Structures." *Materials and Structures* 45: 477–503.
29. Miles, Patrick D, and W Brad Smith. 2009. "Specific Gravity and Other Properties of Wood and Bark for 156 Tree Species Found in North America." *Res. Note. NRS-38*, 35.
30. Millar, Chairman William W, and Port Authority. 1993. *National Cooperative Highway Research Program NCHRP Report 350 Safety Performance Evaluation. Transportation Research*.

31. Nowak, Tomasz P., Jerzy Jasięńko, and Dariusz Czepizak. 2013. "Experimental Tests and Numerical Analysis of Historic Bent Timber Elements Reinforced with CFRP Strips." *Construction and Building Materials* 40: 197–206.
32. Plaxico, Chuck a., Gregory S. Patzner, and Malcolm H. Ray. 2007. "Finite-Element Modeling of Guardrail Timber Posts and the Post-Soil Interaction." *Transportation Research Record: Journal of the Transportation Research Board* 1647 (-1): 139–46.
33. Powell, G H, and Berkeley. Department of Civil Engineering University of California. 1973. *BARRIER VII: A Computer Program for Evaluation of Automobile Barrier Systems*. Federal Highway Administration, Structures and Applied Mechanics Division.
34. Ray, Malcolm H. 1997. "The Use of Finite Element Analysis in Roadside Hardware Design." *International Journal of Crashworthiness*.
35. Santo, Fabio da Silva do Espírito, Milene Maria da Silva-Castro, and Alessandro Rapini. 2012. "Two New Species of Handroanthus Mattos (Bignoniaceae) from the State of Bahia, Brazil." *Acta Botanica Brasilica*.
36. Schümann, Björn. 2010. "Modeling of Soils as Multiphase-Materials with Abaqus." In *2010 SIMULIA Customer Conference*, 1–15.
37. Service, Forest. "Investigating the Use of Small-Diameter Softwood as Guardrail Posts : Static Test Results."
38. Shen, X, L Guo, L Yang, X Du, and P Cao. 2008. "Numerical Analysis of Impact Effect on Mechanical Behavior of Strong Guardrail System." *Journal of Physics: Conference Series* 96: 012036.
39. SIMULIA, and Dassault Systemes. 2015. "Abaqus FEA."

40. Smith, S. T., and J. G. Teng. 2002. "FRP-Strengthened RC Beams. II: Assessment of Debonding Strength Models." *Engineering Structures* 24: 397–417.
41. Tabiei, A, A Svenson, M Hargarvec, and L Bankd. 1998. "Composite Impact Performance of Pultruded Beams for Highway Safety Applications" 42: 231–37.
42. Tabiei, Ala, and Jin Wu. 2000. "Roadmap for Crashworthiness Finite Element Simulation of Roadside Safety Structures." *Finite Elements in Analysis and Design* 34: 145–57.
43. Thiele, Jeffrey, Dean Sicking, Karla Lechtenberg, John Reid, Ronald Faller, Robert Bielenberg, and Scott Rosenbaugh. 2011. "Development of Low-Cost, Energy-Absorbing Bridge Rail." *Transportation Research Record: Journal of the Transportation Research Board* 2262: 107-118.
44. Thiyahuddin, M. I., Y. T. Gu, D. P. Thambiratnam, and H. M. Thilakarathna. 2014a. "Impact and Energy Absorption of Portable Water-Filled Road Safety Barrier System Fitted with Foam." *International Journal of Impact Engineering* 72: 26–39.
45. Valipour, Hamid R., and Keith Crews. 2011. "Efficient Finite Element Modelling of Timber Beams Strengthened with Bonded Fibre Reinforced Polymers." *Construction and Building Materials* 25 (8). Elsevier Ltd: 3291–3300.
46. Whitworth, H A, R Bendidi, D Marzougui, and Reiss R. 2004. "Finite Element Modeling of the Crash Performance of Roadside Barriers." Washington, D.C.: Woodhead Publishing Ltd.
47. Wu, Z., J. Zeng, J. Xiao, and J. Liu. 2014. "Flexural Performance of Integrated 3D Composite Sandwich Structures." *Journal of Reinforced Plastics and Composites* 33 (16): 1496–1507.

48. Yi, Na-hyun, D Ph, Sang-won Lee, Jong-wook Kim, Jang-ho Jay Kim, and D Ph. 2014. "Impact-Resistant Capacity and Failure Behavior of Unbonded Bi-Directional PSC Panels." *International Journal of Impact Engineering* 72. Elsevier Ltd: 40–55.
49. Zachariah, and B U Thomas. 2006. "Finite Element Modelling of Adhesive Interface between Steel and CFRP."

APPENDIX A – ADDITIONAL FIGURES

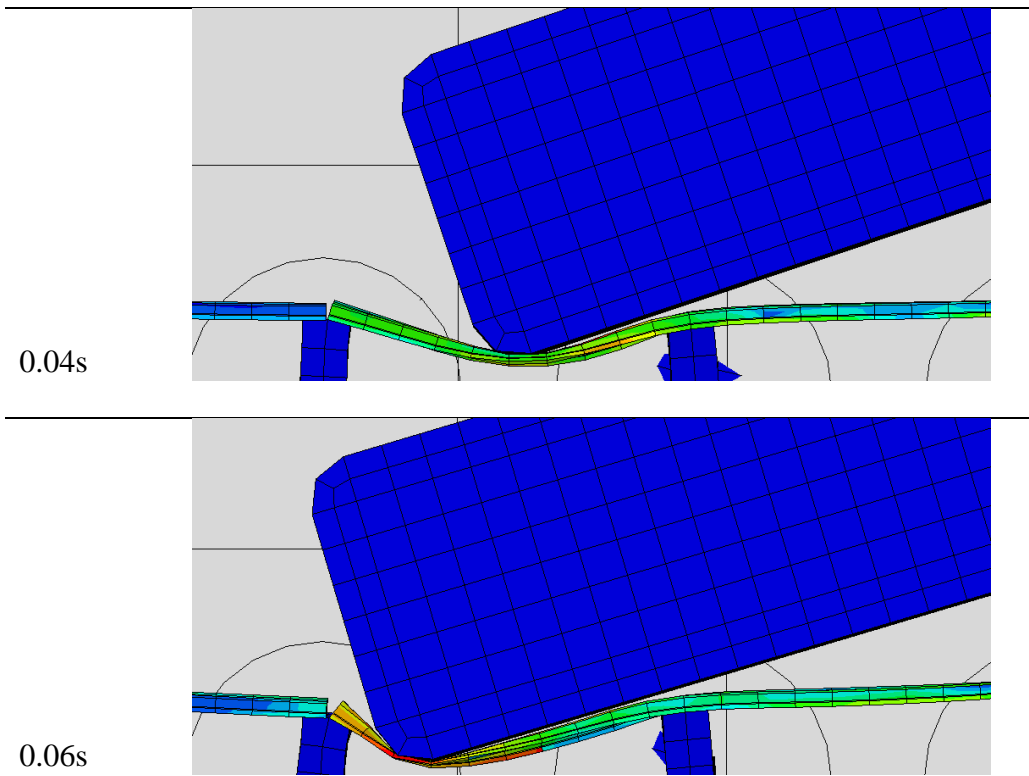


Figure 41: Impact Simulation – Steel W-beam – 1500kg vehicle @ 100km/hr

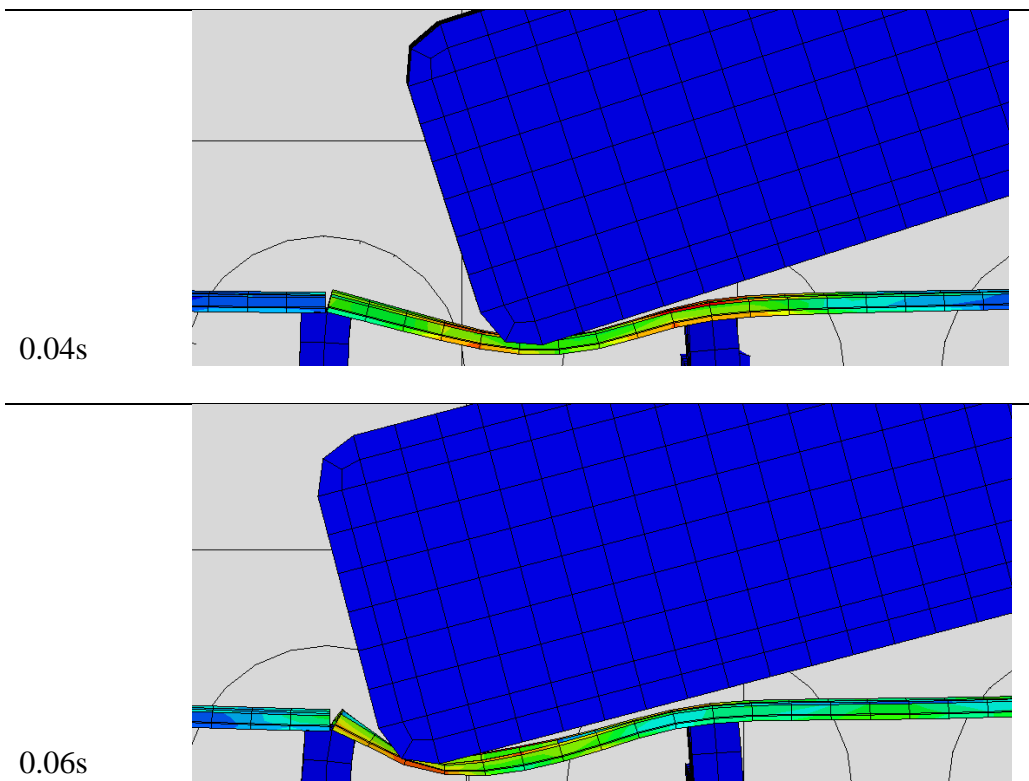


Figure 42: Impact Simulation – Steel W-beam – 895kg vehicle @ 100km/hr

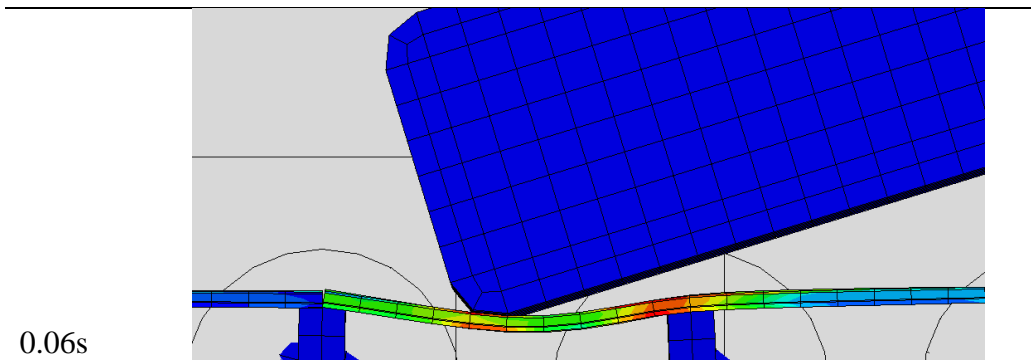
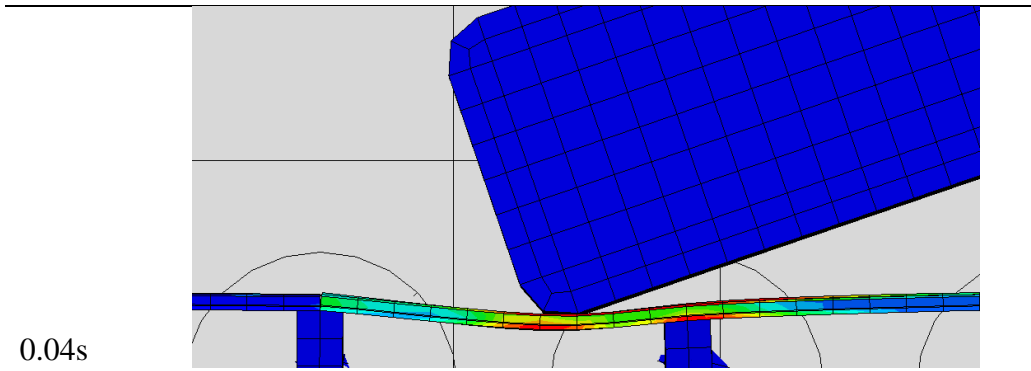


Figure 43: Impact Simulation – Steel W-beam – 895kg vehicle @ 70km/hr

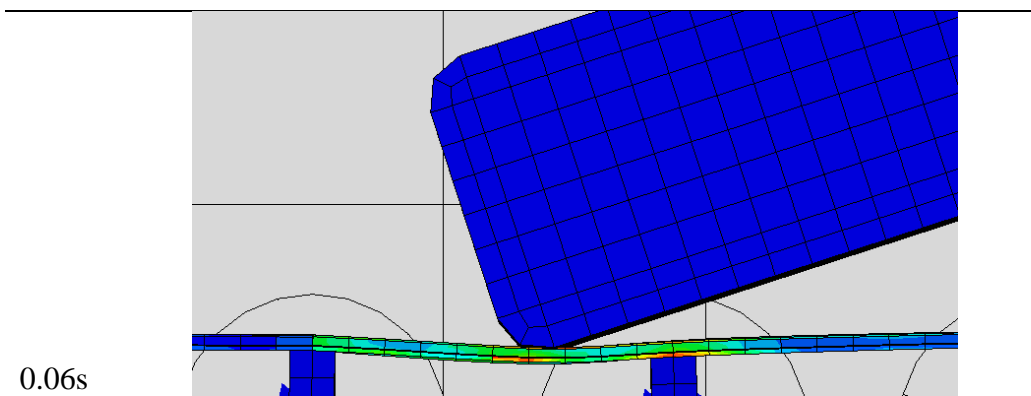
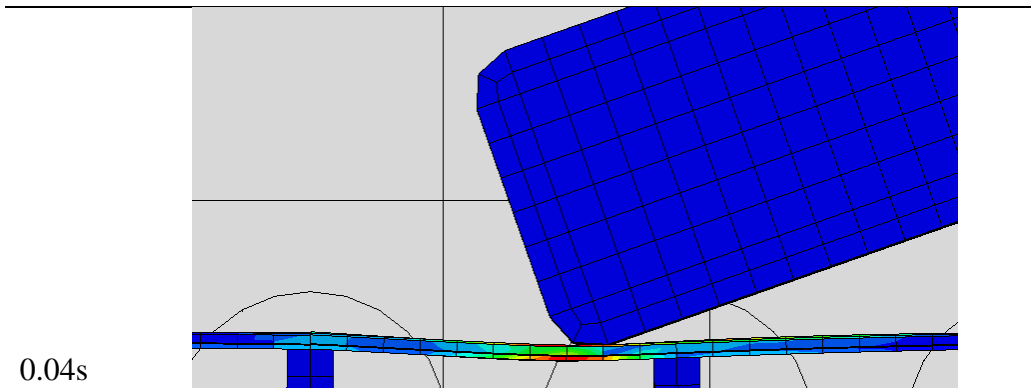


Figure 44 Impact Simulation – Steel W-beam – 895kg vehicle @ 50km/hr

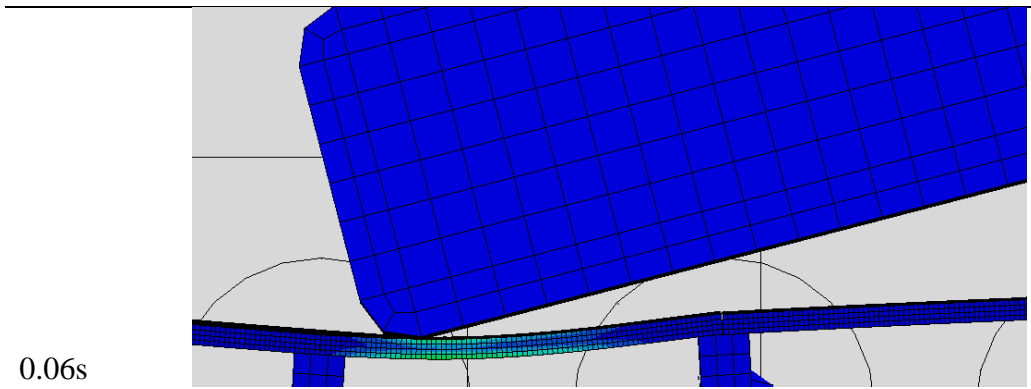
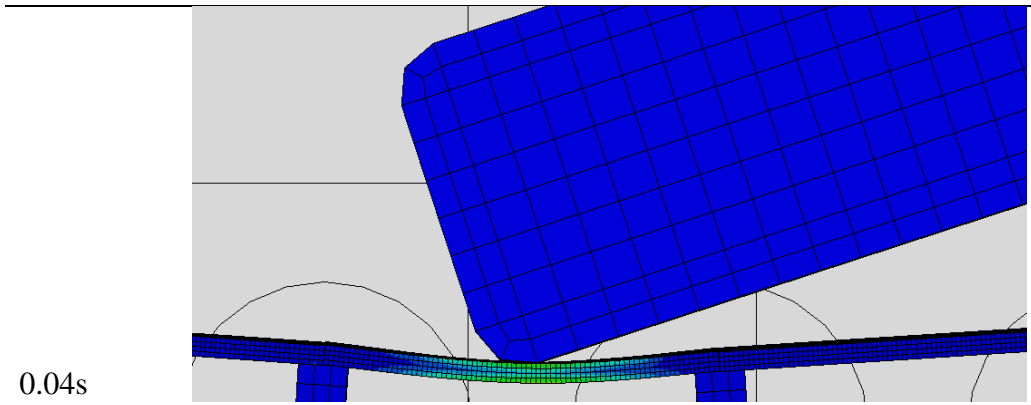


Figure 45: Impact Simulation – IpeA – 1500kg vehicle @ 100km/hr

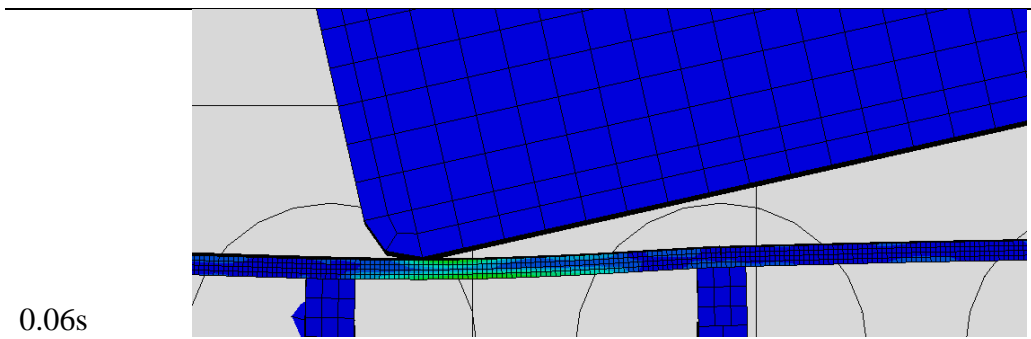
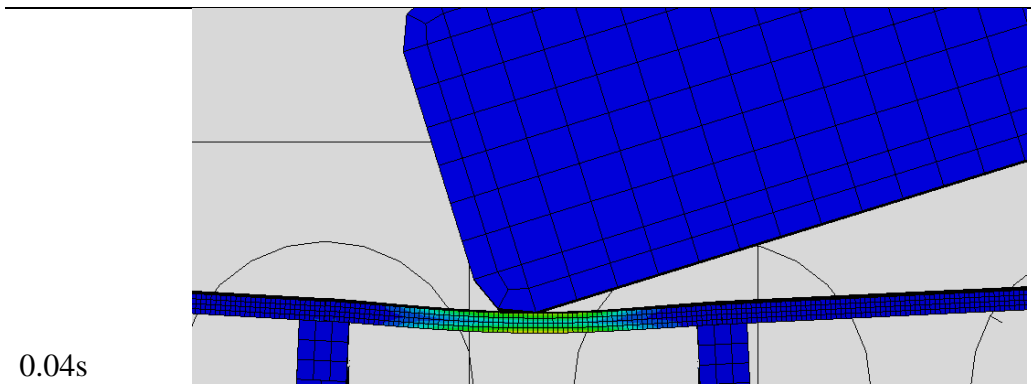


Figure 46: Impact Simulation – IpeA – 895kg vehicle @ 100km/hr

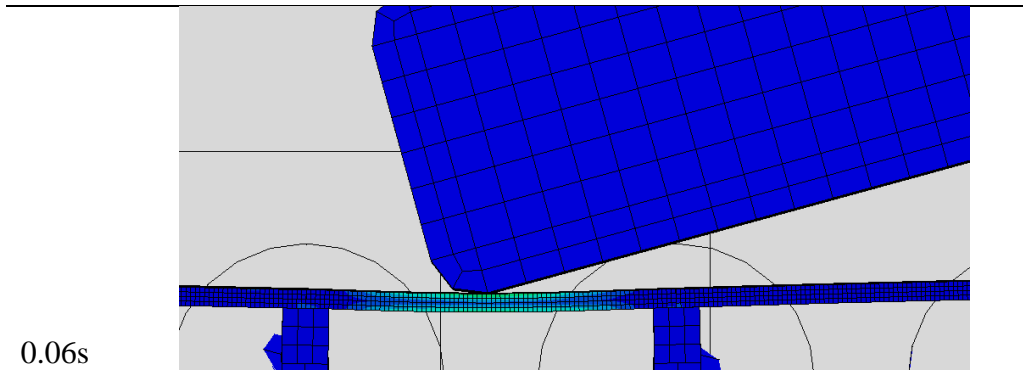
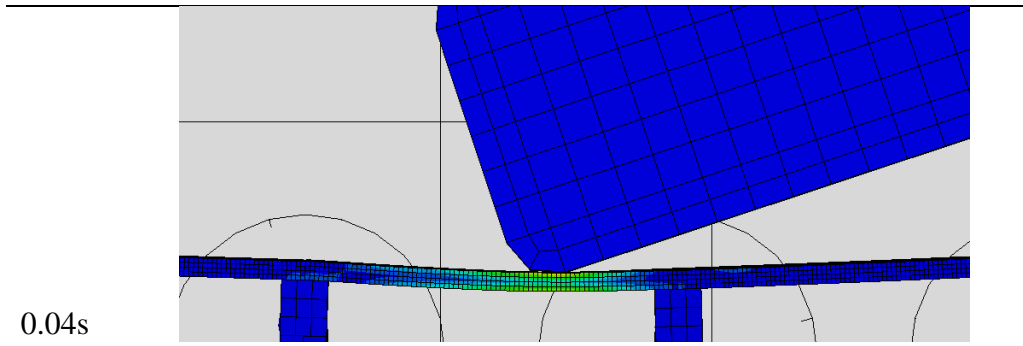


Figure 47: Impact Simulation – IpeA – 895kg vehicle @ 70km/hr

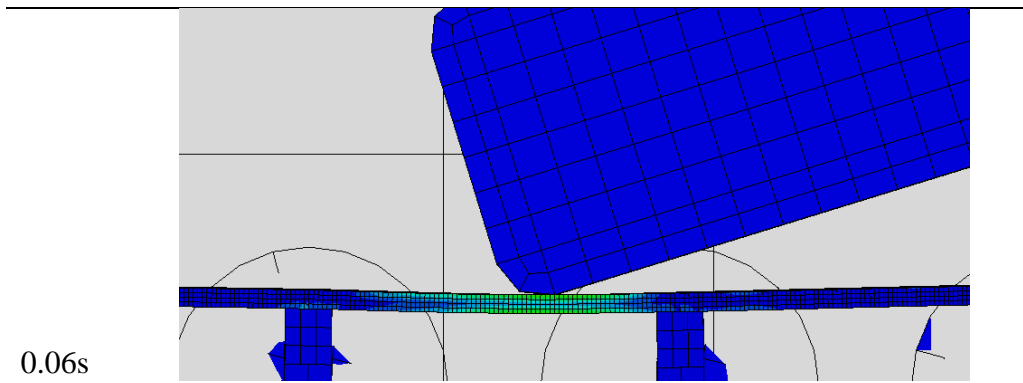
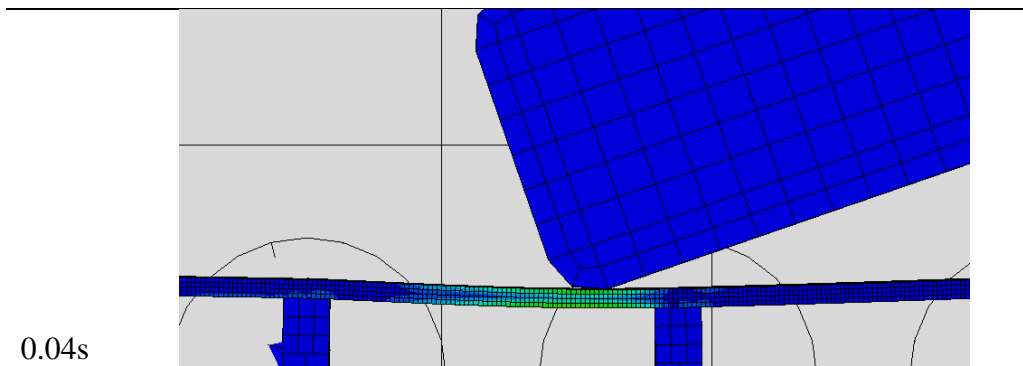


Figure 48: Impact Simulation – IpeA – 895kg vehicle @ 50km/hr

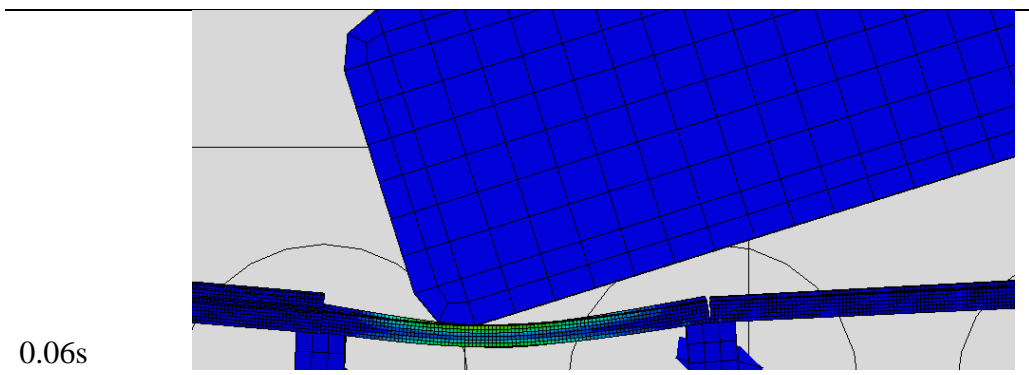
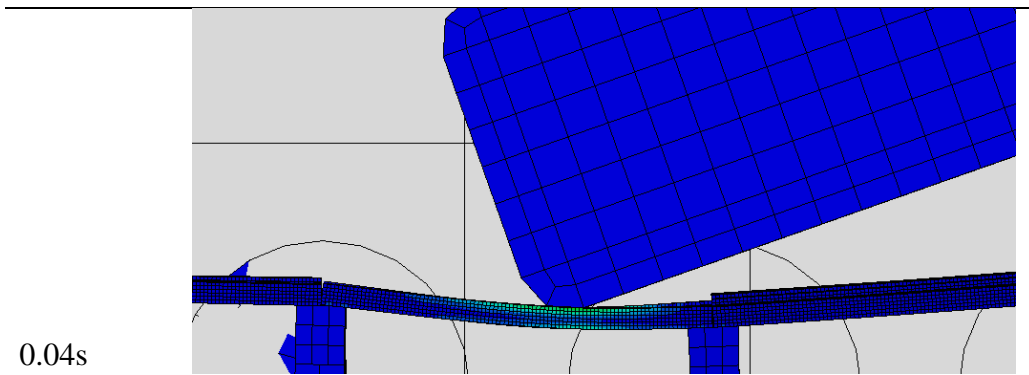


Figure 49: Impact Simulation – IpeD – 1500kg vehicle @ 100km/hr

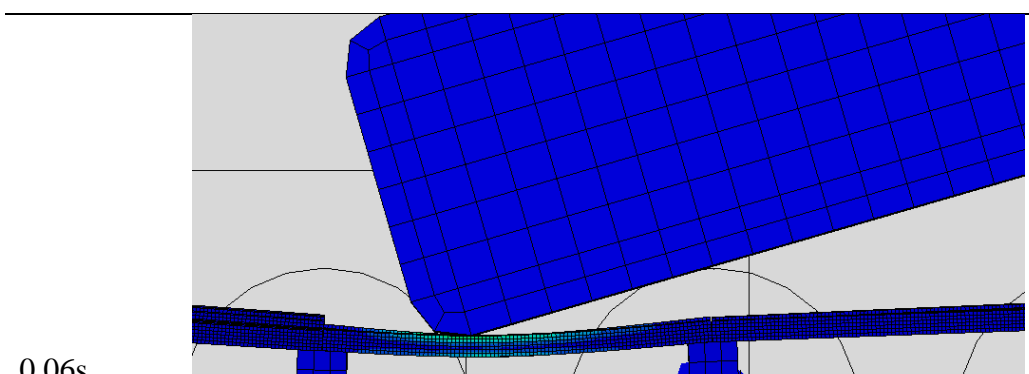
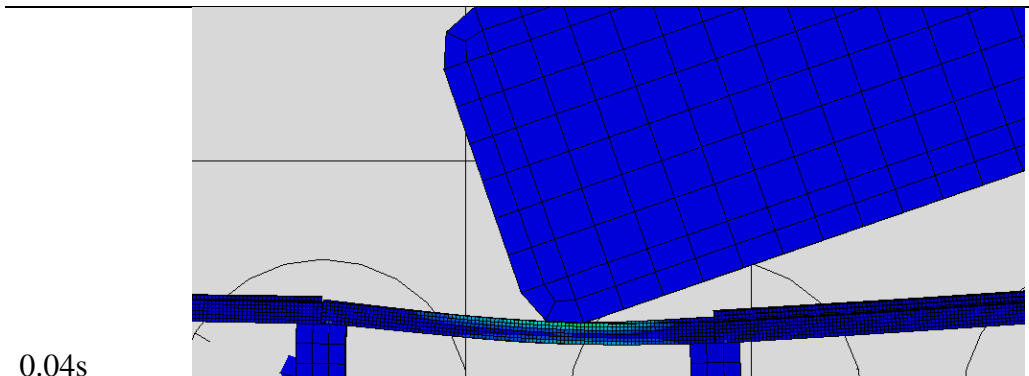


Figure 50: Impact Simulation – IpeD – 895kg vehicle @ 100km/hr

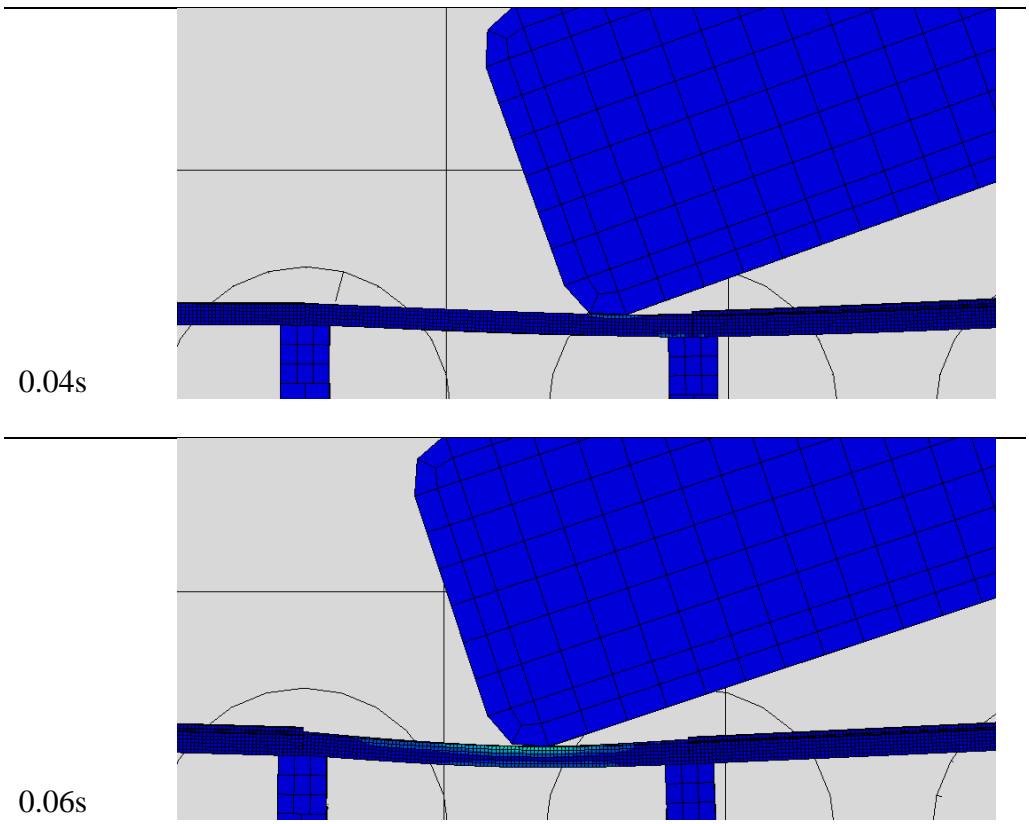


Figure 51: Impact Simulation – IpeD – 895kg vehicle @ 70km/hr

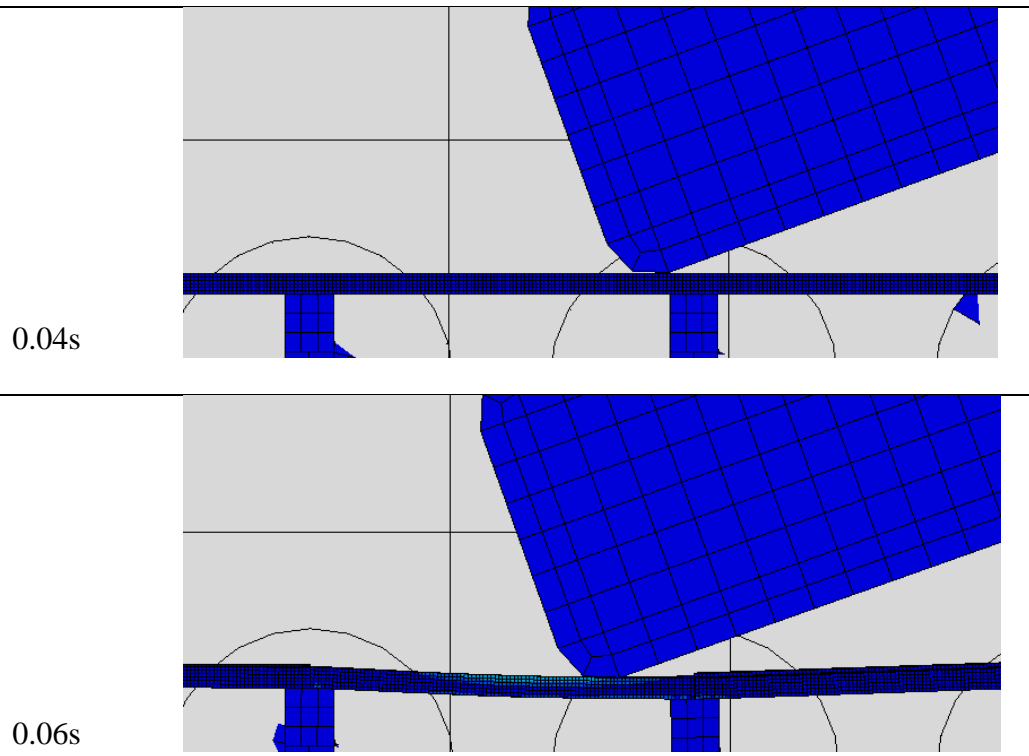


Figure 52: Impact Simulation – IpeD – 895kg vehicle @ 50km/hr

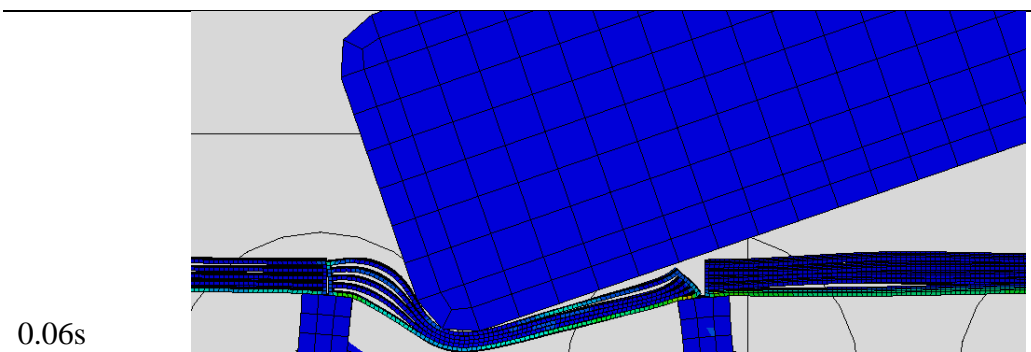
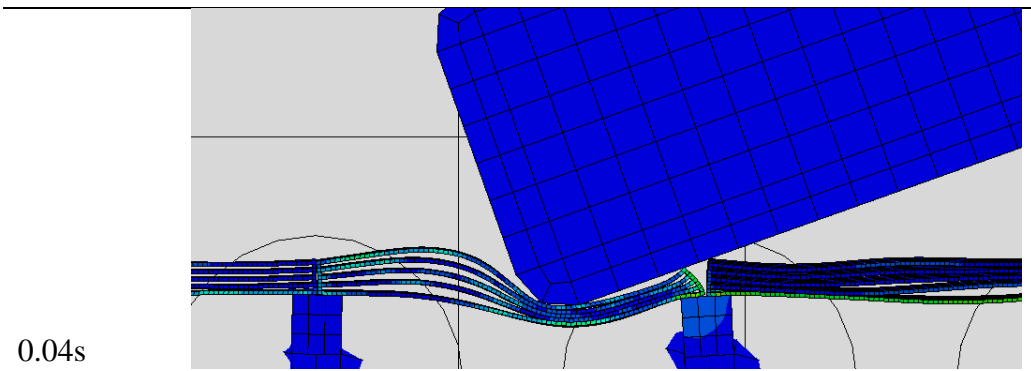


Figure 53: Impact Simulation – IpeE – 1500kg vehicle @ 100km/hr

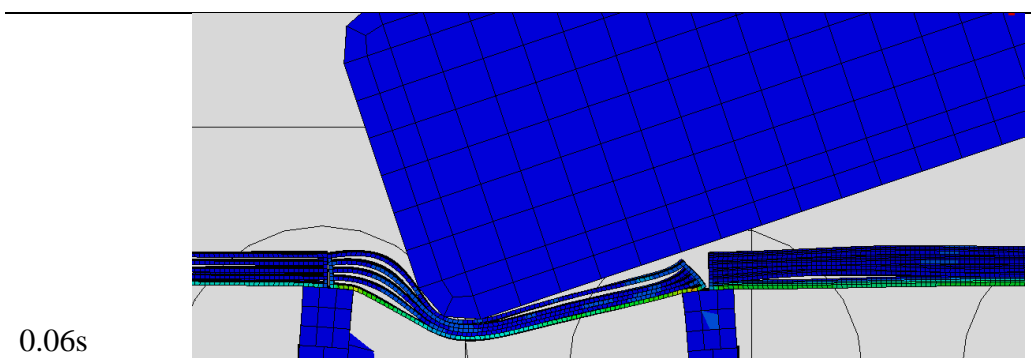
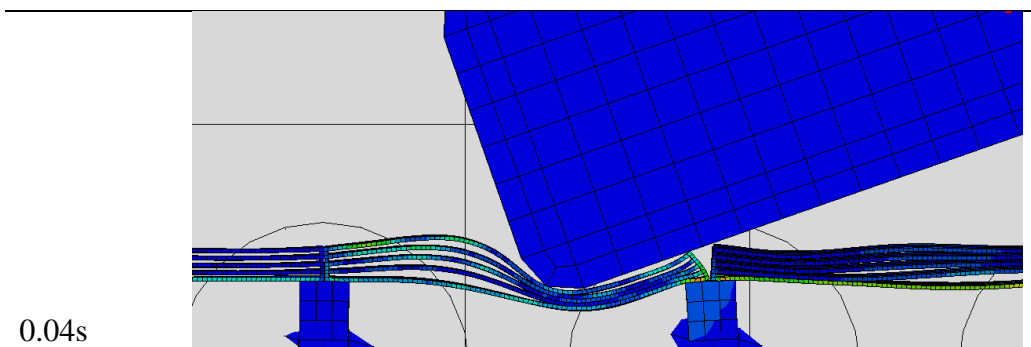


Figure 54: Impact Simulation – IpeE – 895kg vehicle @ 100km/hr

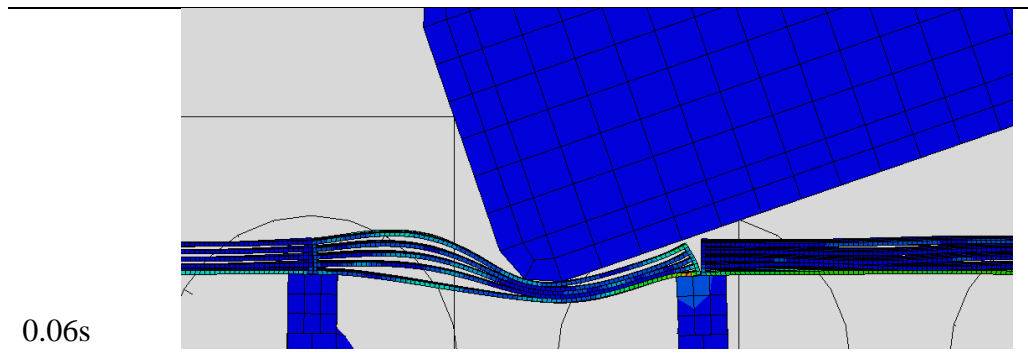
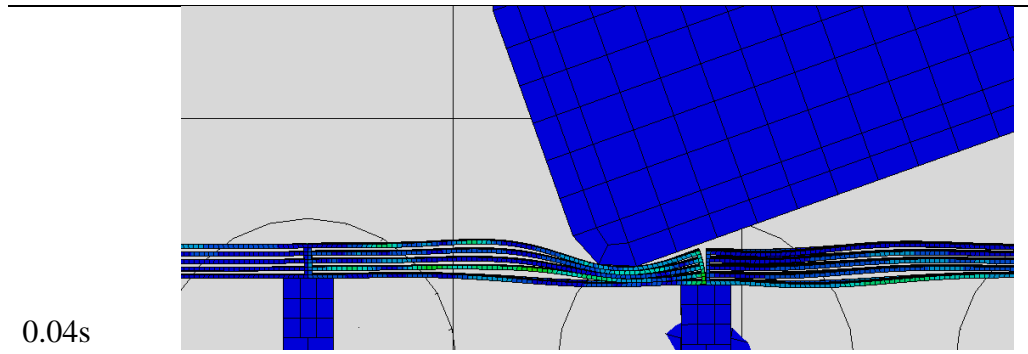


Figure 55: Impact Simulation – IpeE – 895kg vehicle @ 70km/hr

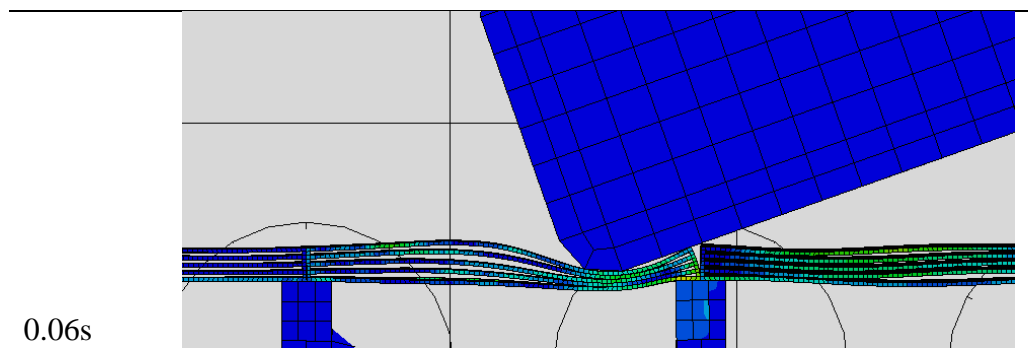
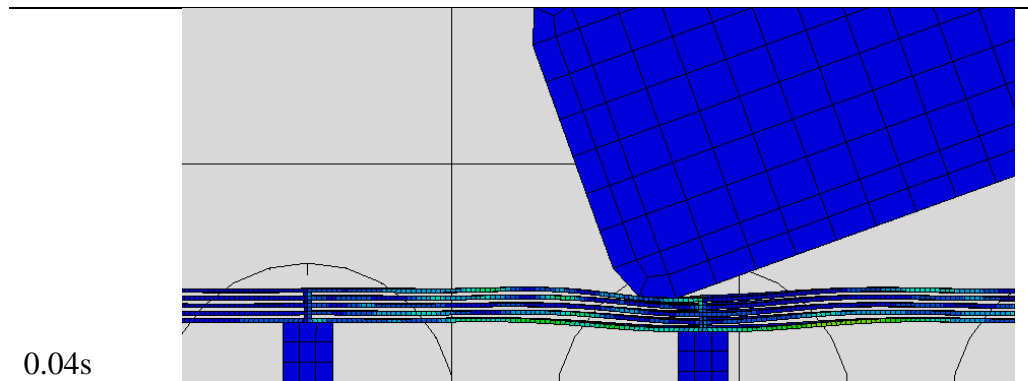


Figure 56: Impact Simulation – IpeE – 895kg vehicle @ 50km/hr